Bulletin of the Seismological Society of America, Vol. 85, No. 6, pp. 1688–1710, December 1995

Simulation of 3D Elastic Wave Propagation in the Salt Lake Basin

by Kim B. Olsen,* James C. Pechmann, and Gerard T. Schuster

Abstract We have used a 3D finite-difference method to model 0.2 to 1.2 Hz elastodynamic site amplification in the Salt Lake Valley, Utah. The valley is underlain by a sedimentary basin, which in our model has dimensions of 48 by 25 by 1.3 km. Simulations are carried out for a *P* wave propagating vertically from below and for *P* waves propagating horizontally to the north, south, east, and west in a two-layer model consisting of semi-consolidated sediments surrounded by bedrock.

Results show that in general, sites with the largest particle velocities, cumulative kinetic energies, duration times of motion, and spectral magnitudes overlie the deepest parts of the basin. The maximum values of these parameters are generally found above steeply dipping parts of the basin walls. The largest vector particle velocities are associated with *P* or *SV* waves that come from within 10° of the source azimuth. Low-energy *S* and surface waves follow the strongest arrivals. The largest peak particle velocities, cumulative kinetic energies, signal durations, and spectral magnitudes in the simulations are, respectively, 2.9, 15.9, 40.0, and 3.5 times greater than the values at a rock site measured on the component parallel to the propagation direction of the incident *P* wave. Scattering and/or mode conversions at the basin boundaries contribute significantly to the signal duration times.

As a check on the validity of our simulations, we compared our 3D synthetic seismograms for the vertically incident plane *P* wave to seismograms of nearly vertically incident teleseismic *P* waves recorded at an alluvium site in the valley and at a nearby rock site. The 3D synthetics for the alluvium site overestimate the relatively small amplification of the initial *P* wave and underestimate the large amplification of the coda. Using 2D simulations, we find that most of the discrepancies between the 3D synthetic and observed records can be explained by an apparently incorrect total sediment thickness, omission from the model of the near-surface low-velocity unconsolidated sediments and of attenuation, and the inexact modeling of the incidence angle of the teleseism. The records from a 2D simulation in which these deficiencies are remedied (with $Q = 65$), and which also includes topography and a near-surface velocity gradient in the bedrock, provide a better match to the teleseismic data than the records from the simple two-layer 3D simulation.

Our results suggest that for steeply incident *P* waves, the impedance decrease and resonance effects associated with the deeper basin structure control the amplification of the initial *P*-wave arrival, whereas reverberations in the near-surface unconsolidated sediments generate the large-amplitude coda. These reverberations are caused mainly by *P*-to-*S* converted waves, and their strength is therefore highly sensitive to the incidence angle of the source.

Introduction

The Salt Lake Valley is a young alluvial valley located at the eastern edge of the Basin and Range Province in north-central Utah (Fig. 1a). This part of Utah has a relatively high level of seismic hazard, based on both historical seismicity and the presence of late Quaternary normal faults (Gori and Hays, 1992). This study addresses one of the most important questions regarding earthquake hazards in the Salt Lake Valley: To what extent will the valley sediments amplify seismic waves from a large nearby earthquake? It is well known that sediment-filled basins amplify ground motion from seismic

*Present address: Institute for Crustal Studies, University of California at Santa Barbara, Santa Barbara, California 93106-1100.

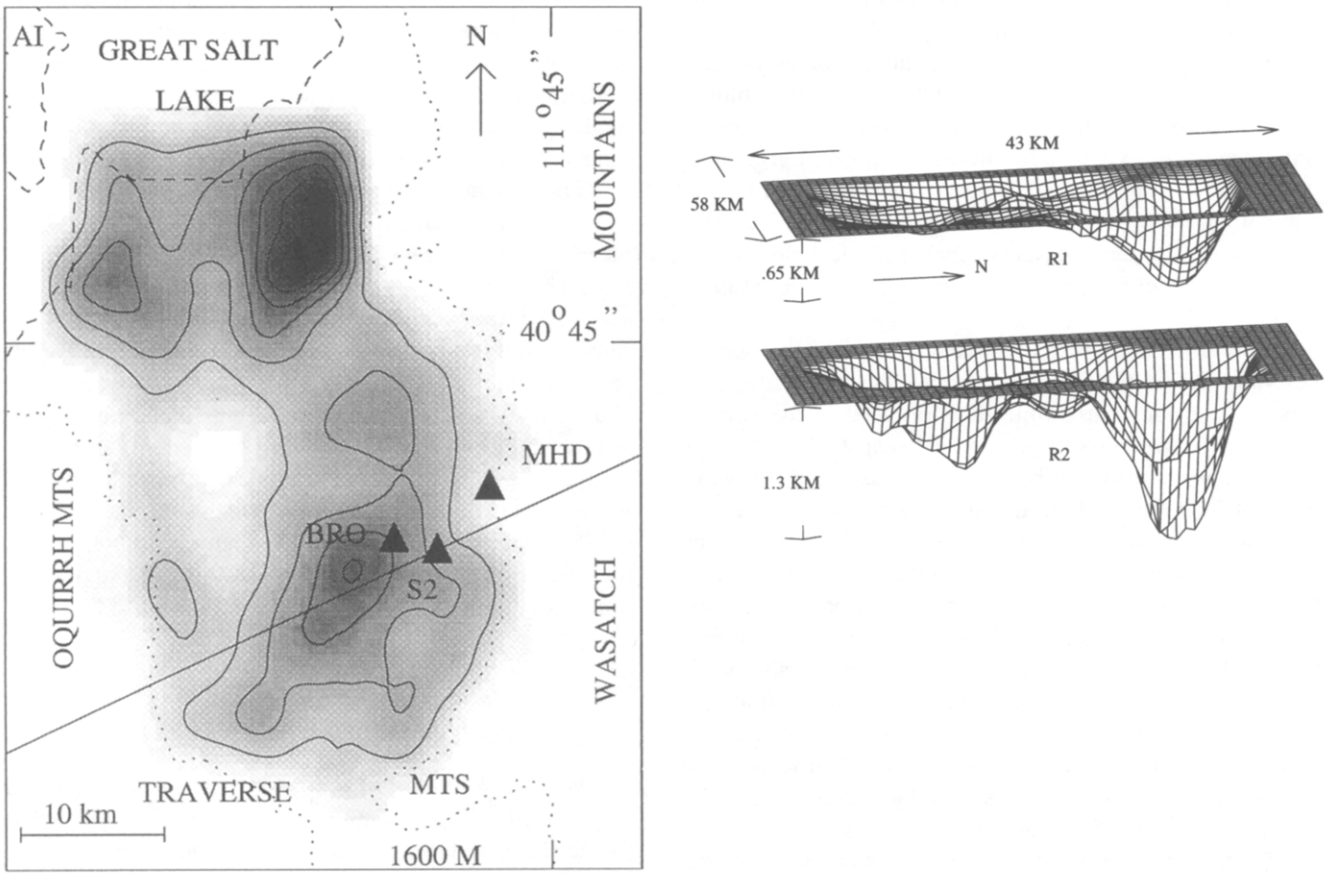

Figure 1. Salt Lake Basin model. (a) Map of the Salt Lake Basin. The contours (200-m interval, shallowest contour at 150 m below the valley floor) and the shading depict the depth of the R2 interface (the sediment-bedrock boundary) below the valley floor; darker shading indicates greater depth to R2. The dotted and dashed lines depict an elevation of 1600 m above sea level and the shoreline of the Great Salt Lake, respectively. AI is Antelope Island; BRO and MHD denote the locations of the two recording sites. The profile and S2 show, respectively, the location of the cross section and a site used in the data comparison section. (b) 3D perspectives of the R1 and R2 interfaces (see text). The 3D modeling parameters are listed in Table 1.

waves relative to the surrounding rock. Therefore, areas underlain by such basins often suffer disproportionate losses of life and property during major earthquakes. Recent examples include the devastation in Mexico City caused by the 1985 M_S 8.1 Michoacan, Mexico, earthquake (Anderson *et al.,* 1986) and the damage caused by the 1989 Loma Prieta, California, earthquake in the cities of San Francisco and Oakland (U.S. Geological Survey Staff, 1990). Such disasters motivate research into the prediction of the locations and magnitudes of the largest ground-motion amplification in alluvial basins. In this article, we use the term "alluvial basin" in a generalized sense to refer to structural basins filled with sediments of various origins, not just fluvial.

Until recently, prediction of ground-motion amplification in alluvial basins was limited to 1D and 2D modeling, for work on the Salt Lake Basin (e.g., Benz and Smith, 1988; Murphy, 1989; Hill *et al.,* 1990; Wong and Silva, 1993; Adan and Rollins, 1993) as well as basins elsewhere (e.g., Bard and Bouchon, 1980a, 1980b; Vidale and Helmberger, 1988; Kawase and Aki, 1989). With the development of more powerful computers, however, it is now possible to extend these amplification analyses to 3D elastic modeling. For example, Frankel and Vidale (1992) simulated 3D elastic waves in the Santa Clara Valley using a far-field *S*-wave source, and Frankel (1993) and Yomogida and Etgen (1993) simulated 3D elastic waves from local earthquake sources in the San Bernardino and Los Angeles Basins, respectively. Though limited to somewhat low-frequency simulations ($\leq$1.5 Hz) due to extensive computational requirements, these studies demonstrated significant 3D effects from the basin structures. These effects include a strong sensitivity of the shaking duration to the location in the basin and the generation of surface waves at the edges of the basin.

This article analyzes ground-motion amplification in the Salt Lake Basin using finite-difference simulations of 3D elastic wave propagation. We use incident *P* waves to ana-

lyze amplification caused by sources different from those used in the other 3D studies mentioned above. Specifically, a vertically incident planar P wave and P waves incident from west, east, north, and south are used to simulate ground-motion amplification in a two-layer 3D model of the Salt Lake Basin. We use a fourth-order staggered-grid finite-difference solution to the 3D elastic wave equation for our simulations. The ground-motion amplification is analyzed using four different measures: peak particle velocity, cumulative kinetic energy, signal duration, and spectral magnitude.

This article is divided into five sections. The first section describes the Salt Lake Basin model, the finite-difference scheme, and the source-time function used in the simulations. In the second section, we use snapshots to analyze wave propagation in the basin for the case of the P wave incident from the south. In the third section, we use a cross-correlation technique to identify the coherent arrivals in the synthetic seismograms and estimate their relative contributions to the amplification. In the fourth section, we describe our amplification measures and discuss the amplification patterns and their relation to the deep basin structure. Finally, as a first check of our 3D simulations, we compare simulated velocity seismograms from a vertically incident plane P wave to recordings of nearly vertically incident teleseismic P waves made at an alluvium site and a bedrock site in the southern part of the Salt Lake Basin.

In the Appendix, we discuss the effect on the simulated ground-motion amplification patterns of interaction of the horizontally propagating P waves with the free surface—a phenomenon that we term "pseudo-geometrical spreading."

Simulation of 3D Wave Propagation

Salt Lake Basin Model

The 3D model of the Salt Lake Basin used in this study (Fig. 1) consists of sediments surrounded by bedrock; the boundary between sediments and bedrock was found by a 3D gravity inversion constrained by three seismic reflection lines and 40 water well logs (Radkins, 1990). The northern (deepest) part of the basin model is the most accurate, because all three seismic reflection lines are located in the northern part of the valley. In the southwestern part of the basin, recent seismic refraction studies suggest that the thickness of the sediments is underestimated by up to 0.4 km in some places (C. Zhou, personal comm., 1993). Radkins (1990) estimated the standard deviation of the sediment thickness in his model to be about 0.25 km.

Hill *et al.* (1990) and Murphy (1989) included three layer boundaries in their 2D Salt Lake Basin models: R1, separating unconsolidated and semiconsolidated sediments; R2, separating semiconsolidated and consolidated sediments; and R3, separating consolidated sediments and bedrock. Their 2D simulations indicate that the dominant features controlling low-frequency amplification in the Salt Lake Valley are the R1 and R2 boundaries. Since the R2 boundary is associated with the biggest impedance contrast, we chose to use this interface—the interface modeled by Radkins (1990)—to separate sediments and bedrock in our model. The unconsolidated sediments are omitted in our 3D model due to the extensive CPU time and memory required to include them.

The density and P-wave velocity of the bedrock are taken from Hill *et al.* (1990), who obtained them from well logs. The sediment P-wave velocity is taken to be 2.2 km/sec, 10% lower than that given by Hill *et al.* (1990) for the semi-consolidated sediments. The lower velocity for the semi-consolidated sediments is an attempt to partially account for the unconsolidated sediments while keeping the sediment velocity within limitations dictated by the available computer resources. S-wave velocities are taken to be the P-wave velocities divided by $\sqrt{3}$. Nicholson and Simpson (1985) found this approximation to be reasonable for bedrock deeper than $\approx$2 to 3 km by analyzing P and S arrival times from microearthquakes; however, they also found that V_p/V_s ratios in rock typically increase to values of around 2.0 at shallower depths.

Finite-Difference Scheme

We use a staggered-grid finite-difference scheme to solve the 3D elastic equations of motion (Levander, 1988); the accuracy is fourth-order in space and second-order in time. The numerical implementation of the 3D scheme is described in Olsen (1994, Chap. 1, Appendix A). The simulations were carried out on an IBM 3090 supercomputer and required approximately 320 Mbytes of physical memory.

The basin model is discretized with a grid spacing of 0.15 km; this corresponds to approximately 7 points per minimum shear wavelength of 1.1 km, which limits the numerical dispersion error to less than 12% (see Olsen, 1994, Chap. 1, Appendix B). The Salt Lake Basin model (approximately 58 by 43 by 9 km) is discretized into 384 by 288 by 60 (=6.6 million) grid points. The sides of the computational model are padded with a zone of attenuative material to limit reflections from the model boundaries (see Olsen, 1994, Chap. 1, Appendix B). The 3D-modeling parameters are listed in Table 1.

We use a Ricker wavelet source in the 3D simulations with a bandwidth of approximately 0.2 to 1.2 Hz (Fig. 2). The planar P-wave sources used in this study were implemented by adding the velocity-time history shown in Figure 2 to the computed particle velocities of the grid points along a plane near the edge of the model.

Analysis of 3D Wave Propagation

In this section, we use snapshots of the E–W-, N–S-, and vertical-component velocities to analyze approximately 20 sec of low-frequency elastic wave propagation in our Salt

Table 1
3D Modeling Parameters

Spatial discretization (km)	0.15
Temporal discretization (sec)	0.013
P-wave velocity of sediments (km/sec)	2.20
S-wave velocity of sediments (km/sec)	1.27
Density of sediments (g/cm^3)	2.2
P-wave velocity of bedrock (km/sec)	5.00
S-wave velocity of bedrock (km/sec)	2.89
Density of bedrock (g/cm^3)	2.6
Number of E–W grid points	288
Number of N–S grid points	384
Number of vertical grid points	60
Minimum source frequency (Hz)	0.2
Maximum source frequency (Hz)	1.2
Peak source frequency (Hz)	0.6
Number of time steps	4616
Simulation time (sec)	60

Lake Basin model for a simulation with a *P* wave incident from the south. The excitation of horizontal motions along a vertical plane generates a *P* wave, an *SV* wave, and a Rayleigh wave due to interaction with the free surface; these waves propagate in the direction of the initial particle motion (see Appendix). The *P* wave causes a strong initial arrival apparent in the snapshots on the N–S and vertical components after 7.8 sec (Fig. 3). The direct arrival propagating in the sediments is delayed compared with that propagating in the surrounding bedrock of higher velocity. The Rayleigh wave generated by the source is much weaker than the direct arrival (see Appendix) and is difficult to identify in the snapshots. Note the region of scattered energy behind the direct arrival on all components within the sediments; this energy is generated by reflections and mode conversions at the basin walls. These mechanisms generate most of the energy on the E–W component, on which the motion from the direct arrival is negligible. By the time the direct arrival enters the northern part of the basin at 10.4 sec, it is weaker than the scattered energy in the southern part of the basin; however, this is in part due to the energy loss from the direct wave caused by pseudo-geometrical spreading (see Appendix).

After the direct wave exits the northern part of the basin at about 15 sec, the strongest ground motion is found at sites above the deepest parts of the basin. The resonating energy in these areas is radiated into the bedrock surrounding the sediments without generating any well-developed, coherent surface waves or trapped body wave phases in the basin. This result contrasts with results from simulations of 3D wave propagation in the San Bernardino (Frankel, 1993) and Los Angeles Basin models (Yomogida and Etgen, 1993). In both of these studies, clear, large-amplitude surface waves were generated at the edges of the basins. In the San Bernardino Basin study, other large, coherent arrivals in the basin were formed by trapped *S* waves multiply reflected between the free surface and the bottom of the basin. Reasons for the contrasting results include differences in the basin models and sources used in the three basin studies. The Salt Lake Basin model differs from Frankel's (1993) San Bernardino Basin model primarily in its impedance contrast between the sediments and bedrock (2.7 in the Salt Lake Basin model, 4.1 and 4.3 in the San Bernardino Basin model for *P* and *S* waves, respectively) and from the Los Angeles Basin model primarily in its sediment thicknesses (deepest point ≈1.3 km for the Salt Lake Basin model and ≈9 km for the Los Angeles Basin model). Bard and Bouchon (1980a, 1980b) showed that basins with relatively small impedance contrasts at the sediment-bedrock interface (comparable to that for the Salt Lake Basin model) are less capable of generating surface waves at basin edges. Hill *et al.* (1990) and Murphy (1989) showed that more energetic surface waves are generated at steeper basin slopes. Relatively shallow sediments and a limited impedance contrast are therefore likely reasons for the relatively weak surface waves encountered in the Salt Lake Basin simulations. Finally, Frankel (1993) and Yomogida and Etgen (1993) both used double-couple sources for their simulations. These sources radiate more *S*-wave energy than *P*-wave energy and may be more likely to excite large-amplitude secondary arrivals than the *P*-wave sources used in this study. Note that the large surface waves observed by Frankel (1993) and Yomogida and Etgen (1993) were generated by *S* waves striking the edges of the basin.

Identification of Arrivals

A critical step in analyzing the causes of ground-motion amplification in the Salt Lake Basin is to estimate the relative contribution to the ground motion from the various phases propagating in the basin. Since visual identification of the phases in the snapshots is complicated by complex 3D wave interference patterns (see previous section) and the vast

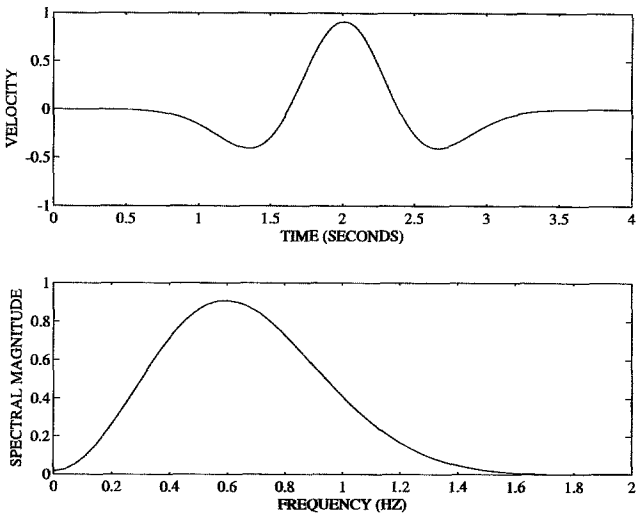

Figure 2. Velocity-time function (top) and velocity spectrum (bottom) of the Ricker wavelet source function used in the 3D simulations.

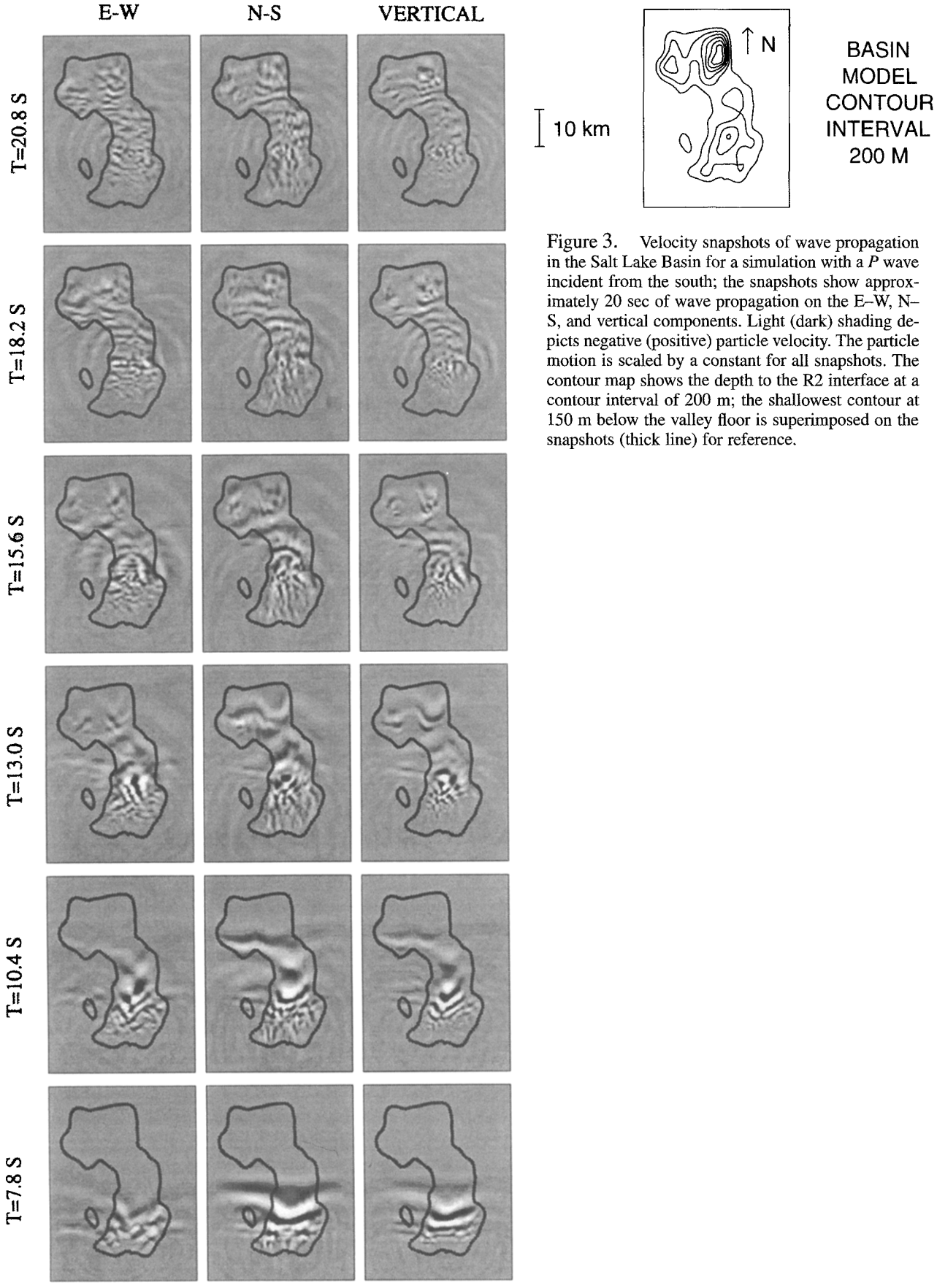

Figure 3. Velocity snapshots of wave propagation in the Salt Lake Basin for a simulation with a *P* wave incident from the south; the snapshots show approximately 20 sec of wave propagation on the E–W, N–S, and vertical components. Light (dark) shading depicts negative (positive) particle velocity. The particle motion is scaled by a constant for all snapshots. The contour map shows the depth to the R2 interface at a contour interval of 200 m; the shallowest contour at 150 m below the valley floor is superimposed on the snapshots (thick line) for reference.

amounts of digital information generated by the 3D simulations (gigabytes!), we use an automatic correlation method to help identify the coherent phases. In this section, we identify the coherent phases in the 3D synthetic records for simulations with a vertically incident plane P wave and P waves incident from the east, west, south, and north in the two-layer Salt Lake Basin model.

Correlation Method

Frankel *et al.* (1991) suggested a cross-correlation method to find the apparent velocities and propagation directions for coherent arrivals in seismograms from a closely spaced array of stations. The method involves calculation of the correlation coefficient C for time windows of two digitized seismograms $V^r(t)$ and $V(t)$ observed at, respectively, a reference point and a nearby site, using the following equation:

$$C(t_0, p_x, p_y) = \frac{\sum_{t=t_0-T}^{t_0+T} V^r(t) \cdot V[t - \Delta t(p_x, p_y)]}{\sqrt{\sum_{t=t_0-T}^{t_0+T} [V^r(t)]^2} \cdot \sqrt{\sum_{t=t_0-T}^{t_0+T} \{V[t - \Delta t(p_x, p_y)]\}^2}}. \quad (1)$$

Here the sums are taken over the windowed time span $2T$ centered at time t_0. C is determined for a range of time lags, $\Delta t(p_x, p_y)$, calculated from a range of possible east–west slowness values p_x and north–south slowness values p_y as follows:

$$\Delta t = p_x \Delta x + p_y \Delta y, \quad (2)$$

where Δx and Δy are the east–west and north–south distances, respectively, between the reference point and the nearby site. The average value of $C(t_0, p_x, p_y)$ for a cluster of stations surrounding the reference site, $\bar{C}(t_0, p_x, p_y)$, is used as a measure of coherency for arrivals propagating with a slowness (p_x, p_y) between times $t_0 - T$ and $t_0 + T$ at the reference station. The slowness vector (p_x^*, p_y^*) associated with the maximum value of $\bar{C}(t_0, p_x, p_y)$ is an estimate of the slowness of the dominant arrivals in that window. The apparent velocity V^a of these arrivals is given by

$$V^a = \frac{1}{\sqrt{p_x^{*2} + p_y^{*2}}}, \quad (3)$$

and the backazimuth ϕ by

$$\phi = \tan^{-1}(p_x^*/p_y^*). \quad (4)$$

We employ a modified version of this method to identify the phases in the records from our 3D simulations. Instead of calculating the cross-correlation for each component separately (equation 1), we compute a normalized sum of inner products (NSIP) for the velocity vectors $\mathbf{V}^r(t)$ and $\mathbf{V}(t)$ as

$$\mathrm{NSIP}(t_0, p_x, p_y) = \frac{\sum_{t=t_0-T}^{t_0+T} \langle \mathbf{V}^r(t), \mathbf{V}(t - \Delta t(p_x, p_y)) \rangle}{\sqrt{\sum_{t=t_0-T}^{t_0+T} \|\mathbf{V}^r(t)\|^2} \sqrt{\sum_{t=t_0-T}^{t_0+T} \|\mathbf{V}(t - \Delta t(p_x, p_y))\|^2}}, \quad (5)$$

where $\| \cdot \|$ and $\langle \cdot, \cdot \rangle$ denote the Euclidean (L^2) norm and the inner product, respectively. This method is based on the same assumptions as the single-component analysis, but the amount of phase information generated is reduced by a factor of 3, and all components of the motion are used to identify the apparent velocity and azimuth of the dominant arrival in each window.

The cross-correlation method finds the slowness vector associated with the largest NSIP value, disregarding any secondary maxima in the NSIP. For example, in Figure 4, the method selects the apparent slowness vector associated with the NSIP value of 0.52 and ignores the apparent slowness vector associated with the local maximum of NSIP = 0.43. This method works well on time/space windows that contain a single dominant arrival. However, if the windows contain two or more strong arrivals with similar waveforms, the method could yield a peak NSIP value that is not associated with the slowness vector of any of these arrivals. Another potential source of discrepancy between the estimated phase velocities and those expected from the model parameters is numerical dispersion error (see Olsen, 1994, Chap. 1, Appendix B).

The likelihood of the cross-correlation method producing spurious results may be minimized by a careful selection of correlation parameters, as discussed in the following section.

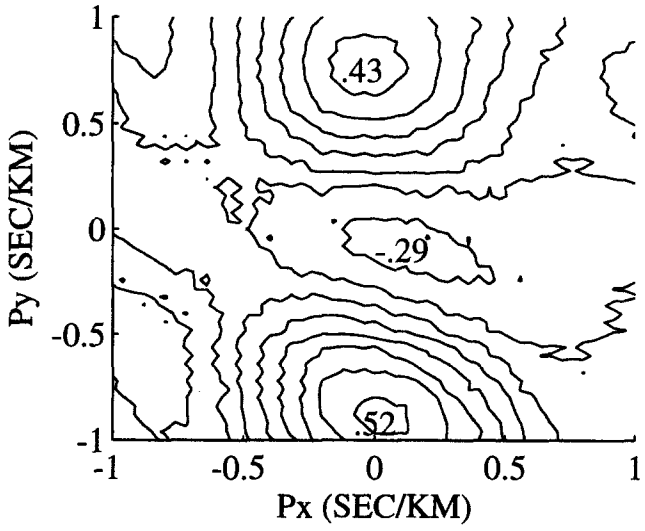

Figure 4. Variation of the normalized sum of inner product (NSIP) with apparent slowness vector for a simulated arrival generated from a P wave incident from the east in the two-layer Salt Lake Basin model. The time window was 1.7-sec long.

Selection of Cross-Correlation Parameters

The cross-correlation method requires selection of the time window length and maximum distance from the reference site for use in applying equation 1 or 5. We choose the maximum distance from the reference site to be approximately half the shear wavelength λ_s, so that the distance between the outermost stations included in the analysis is comparable to λ_s. Similarly, we choose the window length to be equal to the dominant period of the source, which is 1.7 sec. Using larger values for these parameters would make it more likely that the windows would contain multiple arrivals. Smaller values might include only a nonunique fraction of the dominant waveform in the correlation. The potential for error is increased in both cases.

The simulated seismograms were saved at grid points 0.75 km apart, a distance equal to 35% of the dominant wavelength for the *S*-wave energy in the sediments. Thus, of the sites for which we have records, the nearest eight sites to the reference site are at distances of $0.35 \cdot \lambda_s$ to $0.50 \cdot \lambda_s$ and meet our criterion for maximum distance from the reference site. To check this criterion, we use E–W-component seismograms from the simulation with a *P* wave propagating from the east into the two-layer Salt Lake Basin model (Fig. 5). Figure 5a shows the seismograms, and Figure 5b shows the spatial variation of the NSIP values for the nearest 24 stations above the deepest part of the basin (box on map in Fig. 5c) computed for a reference window centered at 33.6 sec. The NSIP values decrease from 0.8 or more at five of the nearest sites to less than 0.4 at most locations two or more grid points from the reference trace; therefore, selection of only the eight stations located nearest the reference trace for the correlation analysis appears to be appropriate. Note that the NSIP value for one or more of the nearby traces can be significantly lower than those of other nearby traces, as occurs SW of the reference site in Figure 5b. For this reason, we use the median NSIP value instead of the mean NSIP value in combining the results from different station pairs, as the median should be less sensitive to isolated regions of lower coherency.

We applied the method to the velocity seismograms obtained from the five 3D simulations at a cluster of nine traces located near the deepest part of the basin (box on the map in Fig. 5c). Unless stated otherwise, the trace spacing is 0.75 km, the time windows are 1.7-sec long, and the overlap between adjacent time windows is 0.7 sec.

Criteria for Phase Identification

In this section, we establish the criteria that we will use to identify the phases found by the cross-correlation analyses of the simulated seismograms.

The apparent velocity of a phase provides the first clue to its identity. Apparent *P*- and *S*-wave velocities at the sites used in the cross-correlation analyses must be greater than or equal to 2.2 and 1.27 km/sec, respectively—the true *P*- and *S*-wave velocities of the underlying sediments (Table 1). Surface-wave velocities at these sites will vary somewhat with frequency and sediment thickness. As the range of sediment thicknesses beneath these sites is relatively small, 0.9 to 1.2 km, we assume that the variation of surface-wave velocities with sediment thickness is negligible and determine average surface-wave velocities with a model consisting of a 1.05-km-thick layer of sediments over a half-space of bedrock. A 2D simulation using this model and our Ricker wavelet source showed that Rayleigh-wave velocities vary between 1.1 and 1.3 km/sec; this finding indicates that the bedrock does not significantly affect the Rayleigh-wave velocities in this area. This result is expected because the Rayleigh-wave velocity is generally considered sensitive to velocities down to depths of about one-third of the shear wavelength (e.g., Stacey, 1992, p. 216), and in our case, the mean shear wavelength is 2.1 km. For Love waves, we showed analytically (see Aki and Richards, 1980, p. 262) that fundamental-mode phase velocities in our layer-over-half-space model range between 1.34 and 2.13 km/sec for frequencies of 0.3 to 0.9 Hz, the range covered by our simulations. The first higher-mode Love wave exists within this bandwidth but is expected to be less important than the fundamental mode (see Bard and Bouchon, 1980a).

Apparent velocity alone does not usually enable unambiguous phase identification. We therefore utilize particle motions to help constrain our interpretations. Here, in addition to particle motion plots, we use the average kinetic energy within 1.7-sec-long time windows on the vertical, E–W, and N–S components at the nine sites included in the analysis. We compute the kinetic energy per unit volume at each time step by

$$\frac{1}{2}\rho \dot{u}_k^2(t), \tag{6}$$

where $\dot{u}_k(t)$ is the velocity on the kth component at time t and ρ is density. The average of this quantity was computed for the windowed seismograms corresponding to the largest values of NSIP. With apparent velocity, backazimuth, and particle motion information available, we can use the criteria summarized in Table 2 to identify the coherent phases in the synthetic records. To prevent nonphysical results for time windows containing multiple arrivals, we constrained the correlation method to only select arrivals with apparent velocities larger than 1.0 km/sec.

Summary of Phase Identification for the Simulations

Figure 6 shows the results of our cross-correlation analyses of synthetic seismograms from the boxed area in Figure 5c for three of our five simulations: those for *P* waves incident from the east and south and for the vertically incident *P* wave (the results for *P* waves incident from the north and west are shown in Olsen, 1994). Our main conclusions from these analyses may be summarized as follows:

1. All of the first arrivals have apparent velocities larger

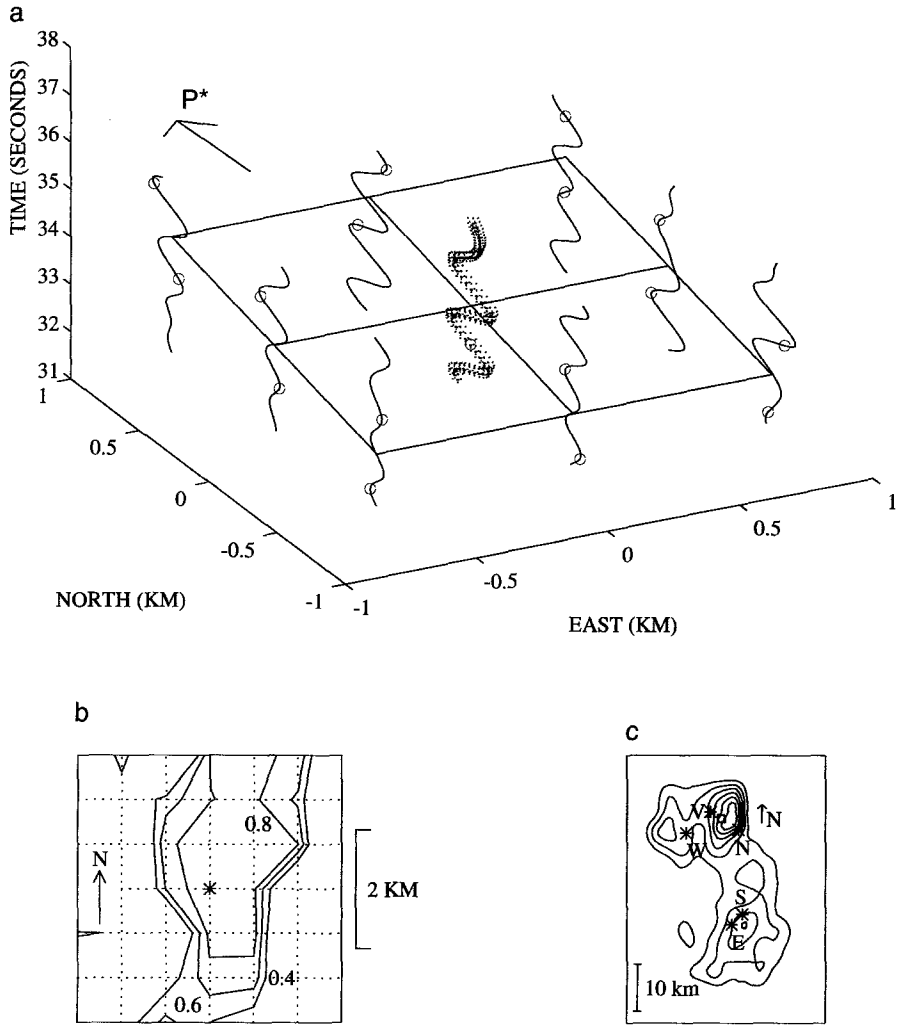

Figure 5. Illustration of phase identification method. (a) Identification using our correlation method for an arrival with apparent slowness vector **p*** (shown by the arrow); the simulation is for a *P* wave incident from the east in the two-layer basin model. The thick trace represents the reference trace in the correlation. The plane superimposed on the seismograms connects the arrival on the reference trace and the eight surrounding traces. The first and last samples of the windowed traces are depicted by circles. (b) Spatial variation of the NSIP values calculated for a time window centered at 33.6 sec from the recordings at 24 stations located around the reference trace (*) at the intersections of the dotted lines. (c) Contour map showing the depth to the R2 interface at a contour interval of 200 m, shallowest contour at a depth of 150 m below the valley floor; the square depicts the location of the stations used for the phase identification. The locations of the strongest arrivals for the simulations with *P* waves incident from the east, west, north, south, and vertical directions are depicted by E, W, N, S, and V, respectively.

than 3.5 km/sec, which, together with their backazimuths and first motions, indicates that they are steeply incident *P* waves that have initially traveled through the bedrock and then have been refracted upward into the sediments.

2. Beginning 4 to 6 sec after the initial *P* wave, nearly all of the dominant arrivals have apparent velocities less than 2.2 km/sec, the *P*-wave velocity of the sediments in the basin model. Therefore, these later arrivals must be *S* waves and/or surface waves.
3. In all of the simulations except for the one with the *P* wave incident from the south, most of the seismic energy arrives during the first 10 sec after the first arrival.
4. For the simulations with the *P* waves incident from the east (Fig. 6), north, and west, the cross-correlation analyses show that the dominant arrivals are from the source direction for only 6 to 9 sec after the first arrival.
5. For the simulation with the *P* wave incident from the south, the dominant arrivals continue to come from the general direction of the source for more than 30 sec after the initial *P* wave. The incoming seismic energy remains

Table 2
Phase Identification Criteria

Apparent Velocity (km/sec)	Particle Motion Relative to Propagation Direction	Phase
1.27–1.34	transverse	*SH*
1.34–2.13	transverse	*SH* or Love
>2.13	transverse	*SH*
1.1–1.3	retrograde elliptical	Rayleigh
1.27–2.2	radial and/or vertical	*SV*
≳2.2	radial and/or vertical	*P* or *SV*

high for this entire 30-sec time span. The longer train of energy from the source direction for the case of the *P* wave incident from the south is probably due to the longer propagation path from the edge of the basin to our reference site (45 km versus 20 km or less) and the associated generation of converted and scattered phases along this path.

6. Some Rayleigh waves are generated in the basin (e.g., at 10 sec in the simulation with the vertically incident *P* wave), and perhaps Love waves. However, Love waves cannot be unambiguously identified with the methods we used.

Figure 6 shows that several wave types contribute to the strongest ground motions 2 km west of the deepest part of the Salt Lake Basin. To determine the types of phases that cause the strongest motions in the valley as a whole, we applied our cross-correlation technique to the synthetic seismograms at and around the sites where the largest peak vector particle velocities in the entire valley occurred during each of the five *P*-wave simulations. The locations of these sites are depicted on the map in Figure 5c, and the arrivals are described in Table 3. The largest vector particle velocities are caused by *P* waves when the source wave is vertically incident and by *SV* waves when the source wave is incident from the east, west, and south. It is not surprising that these phases are among the most energetic arrivals, because a horizontally incident *P* wave generates a *P* wave, an

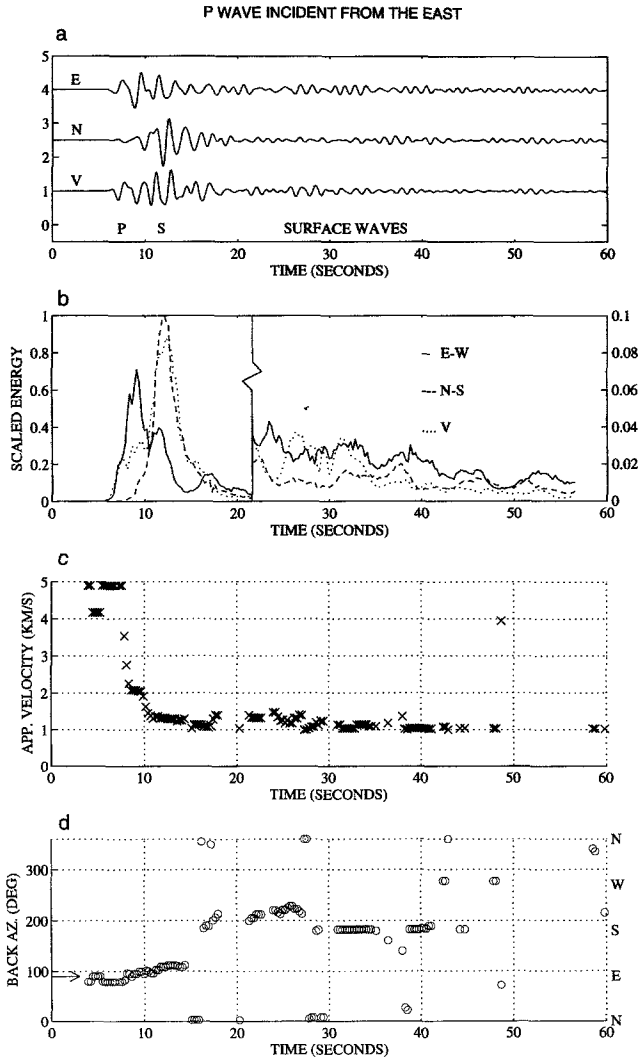

Figure 6. Phase identification above the deepest part of the basin model (the area within the square shown in Fig. 5c) for simulations with *P* waves incident from the east and south, and with a vertically incident *P*-wave. (a) Plots of velocity seismograms calculated at the reference station, (b) normalized kinetic energy on the E–W, N–S, and vertical components; the kinetic energies shown are average values over 1.7-sec time windows computed for the reference station and the eight surrounding stations. The identified phases are labeled below the seismograms. The kinetic energy is shown at two different scales; the left (right) axis corresponds to the parts of the curves left (right) of the jump. (c) Plots of apparent velocity and (d) backazimuth values associated with the highest values of NSIP. The arrow denotes the azimuth to the source. Apparent velocities and backazimuths for arrivals with apparent velocities larger than 5 km/sec are not shown.

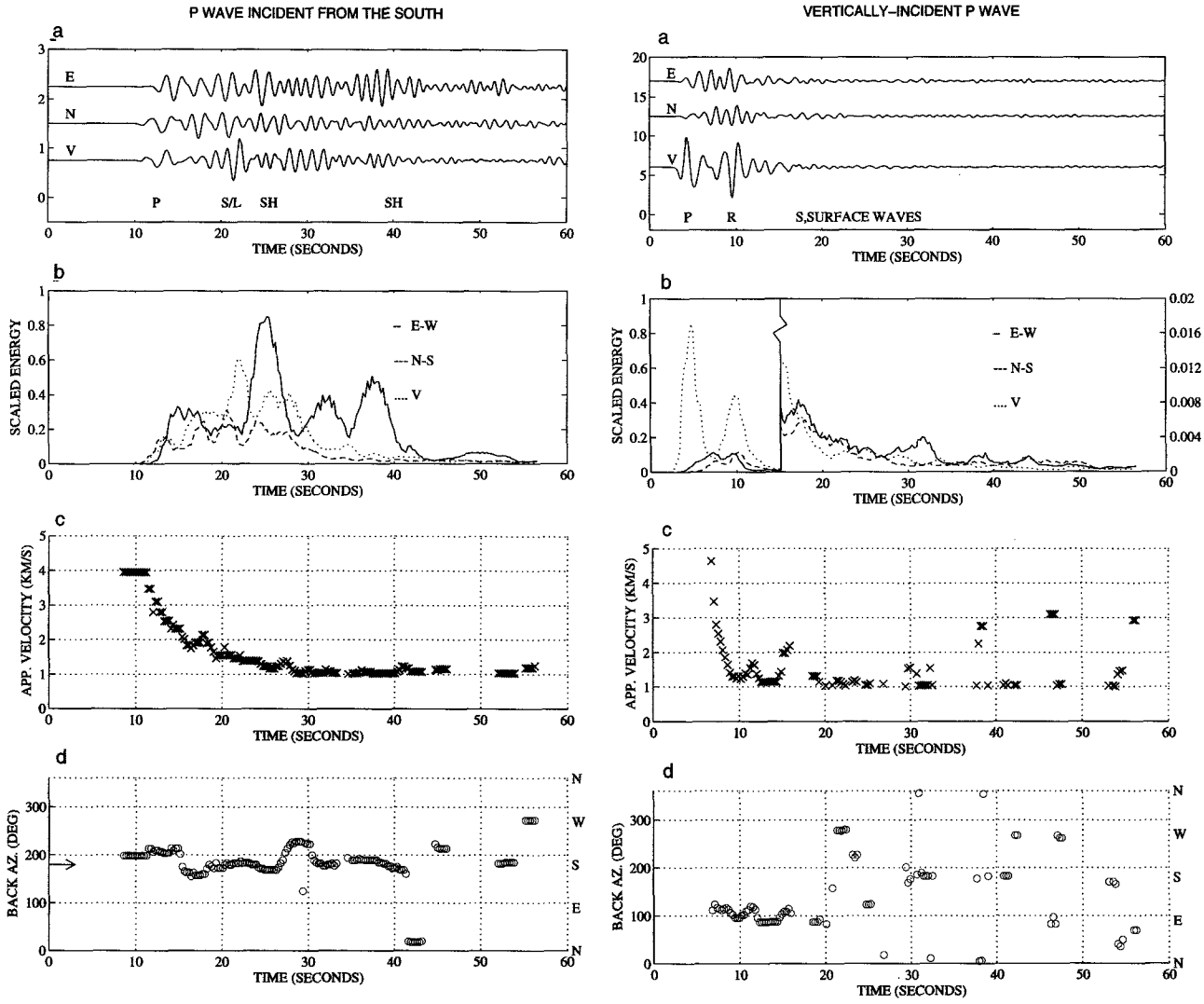

Figure 6. Continued

SV wave, and a Rayleigh wave (see Appendix). Note, however, that the source wave type, a *P* wave, causes the largest motions only when the source is vertically incident. For at least three out of the four simulations with horizontally incident *P* waves, the largest ground motions are caused by *S* waves. This finding suggests that *P*- to *S*-wave conversion contributes significantly to ground-motion amplification in the two-layer Salt Lake Basin model, in agreement with the results of Olsen and Schuster (1995).

In the simulations with the horizontally incident *P*-wave sources, the arrivals that generate the largest vector velocities at the surface of the basin model come from within 10° of the source azimuth (Table 3). All of these phases arrive less than 20 sec after the *P* waves enter the Salt Lake Basin (Table 3). Figure 6 shows that for these simulations, the most energetic arrivals in our study area 2 km west of the deepest part of the Salt Lake Basin also come primarily from the source azimuth.

Basin Amplification Patterns

In this section, we present maps of the ground-motion amplification patterns in the Salt Lake Basin produced by our finite-difference simulations. We use ratios of four different ground-motion parameters to characterize the amplification patterns: peak particle velocity, cumulative kinetic energy, spectral magnitude in the bandwidth 0.2 to 1.2 Hz, and signal duration.

Definition of Ground-Motion Parameters

The four ground-motion parameters are defined as follows:

1. The peak particle velocity measured at location (x, y) for the kth component is defined as

$$P_k(x, y) = \text{MAX}(|\dot{u}_k(x, y, t)|), \quad (7)$$

Table 3
Arrivals Causing the Largest Vector Peak Particle Velocities in the Salt Lake Valley

Source Direction	Arrival Time (sec)*	Apparent Velocity (km/sec)	Back azimuth (°)	Wave Type
East	11.2	3.1	90	*SV*
North	16.0	1.5	350	unknown
West	8.4	3.1	263	*SV*
South	12.0	3.1	173	*SV*
Vertical	4.2	12.5	270	*P*

*Measured from the start of the simulation.

where $\dot{u}_k(x, y, t)$ is the velocity time history for the kth component and MAX indicates the maximum value of $|\dot{u}_k(x, y, t)|$ for all time t.

2. The cumulative kinetic energy per unit volume for the kth component is given as

$$E_k(x, y) = \frac{1}{2} \rho(x, y) \int \dot{u}_k^2(x, y, t)dt, \quad (8)$$

where $\rho(x, y)$ is the density and the limits of integration are over the time interval of the simulation.

3. The signal duration is the time interval from the *P*-wave arrival to the beginning of the first interval when the absolute value of the velocity averaged over 1 sec stays below 7.5% of the peak source velocity for 2.6 consecutive sec.

4. The spectral magnitude of the kth component is defined as

$$S_k(x, y, \omega) = |\dot{U}_k(x, y, \omega)|, \quad (9)$$

where $\dot{U}_k(x, y, \omega)$ is the temporal Fourier transform of $\dot{u}_k(x, y, t)$. The last 5 sec of the seismic traces are tapered by a Hanning window prior to transformation into the frequency domain. The mean spectral magnitude is found by averaging the spectrum between 0.2 and 1.2 Hz.

The ground-motion parameters are normalized to those measured at a rock site on the component parallel to the propagation direction of the incident *P* wave; for the horizontally incident *P* waves, this site is located 3 km from the plane where the source is imposed. The distance from the observation point to the reference point for the horizontally incident *P* waves should be considered when analyzing the simulated ground-motion parameters, since the *P*-wave energy decays in the propagation direction. This energy loss is caused by *P*- to *S*-wave conversion along the free surface, and we will refer to it as pseudo-geometrical spreading in the following text. Pseudo-geometrical spreading causes the peak particle velocity to decay by 90% during propagation through 35 km of a half-space of basin sediments (see Appendix).

Figure 7. (On following pages.) Maps of ground-motion parameters on the E–W, N–S, and vertical components for simulations with *P* waves propagating into the two-layer model in the directions indicated at the left of each row. From top to bottom, the *P* waves enter the model from the east, north, south, west, and vertically from below. The ground-motion parameters are normalized to their value at a rock site on the component parallel to the propagation direction of the incident *P* wave. For the horizontally incident *P* waves, this site is located 3 km from where the source is imposed. The reference site for the vertically incident *P* wave is labeled "C" on the contour map. Closed contour lines shorter than approximately 16 km are considered beyond the resolution of the modeling and have been discarded from the plot. The contour map at the bottom right shows the depth to the R2 interface at a contour interval of 200 m; the shallowest contour at 150 m below the valley floor is superimposed on the maps (thick line) for reference.

Ground-Motion Parameter Ratios in the Salt Lake Basin

Figure 7 shows maps of the normalized peak particle velocity, cumulative kinetic energy, signal duration, and mean spectral ratio from 0.2 to 1.2 Hz for the five *P*-wave simulations with the two-layer model. These maps demonstrate the effect of the deep 3D basin structure of the Salt Lake Basin on site amplification. The largest values of all four ground-motion parameters generally occur above or near the deepest parts of the basin for all of the simulated source incidence angles. This result is consistent with the results of the 2D simulations of Hill *et al.* (1990) for *SH* waves and Murphy (1989) for *P* and *SV* waves. To illustrate this point more clearly, Figure 8 shows the locations where the largest values of the ground-motion parameters are found. Note that none of these sites are located directly above local maxima in the basin depths. Instead, the sites with the maximum ground motions are concentrated *near* the deepest points of the basin where the slopes of the underlying basin floor are relatively large.

Table 4 shows that the peak particle velocities, cumulative kinetic energies, signal durations, and spectral magnitudes are amplified by factors of 0.9 to 2.9, 1.8 to 15.9, 19.6 to 40.0, and 1.2 to 3.5, respectively. The lower-amplification factors generally occur on components perpendicular to the direction of the source. The energy on these components comes primarily from *P*- to *S*-wave conversion, surface-wave generation, and lateral refraction by the basin structure.

The spatial variation of the ratios of particle velocities, cumulative kinetic energies, and mean spectral magnitudes for the horizontally incident *P* waves is caused by a combination of pseudo-geometrical spreading and basin amplification effects. The pseudo-geometrical spreading causes

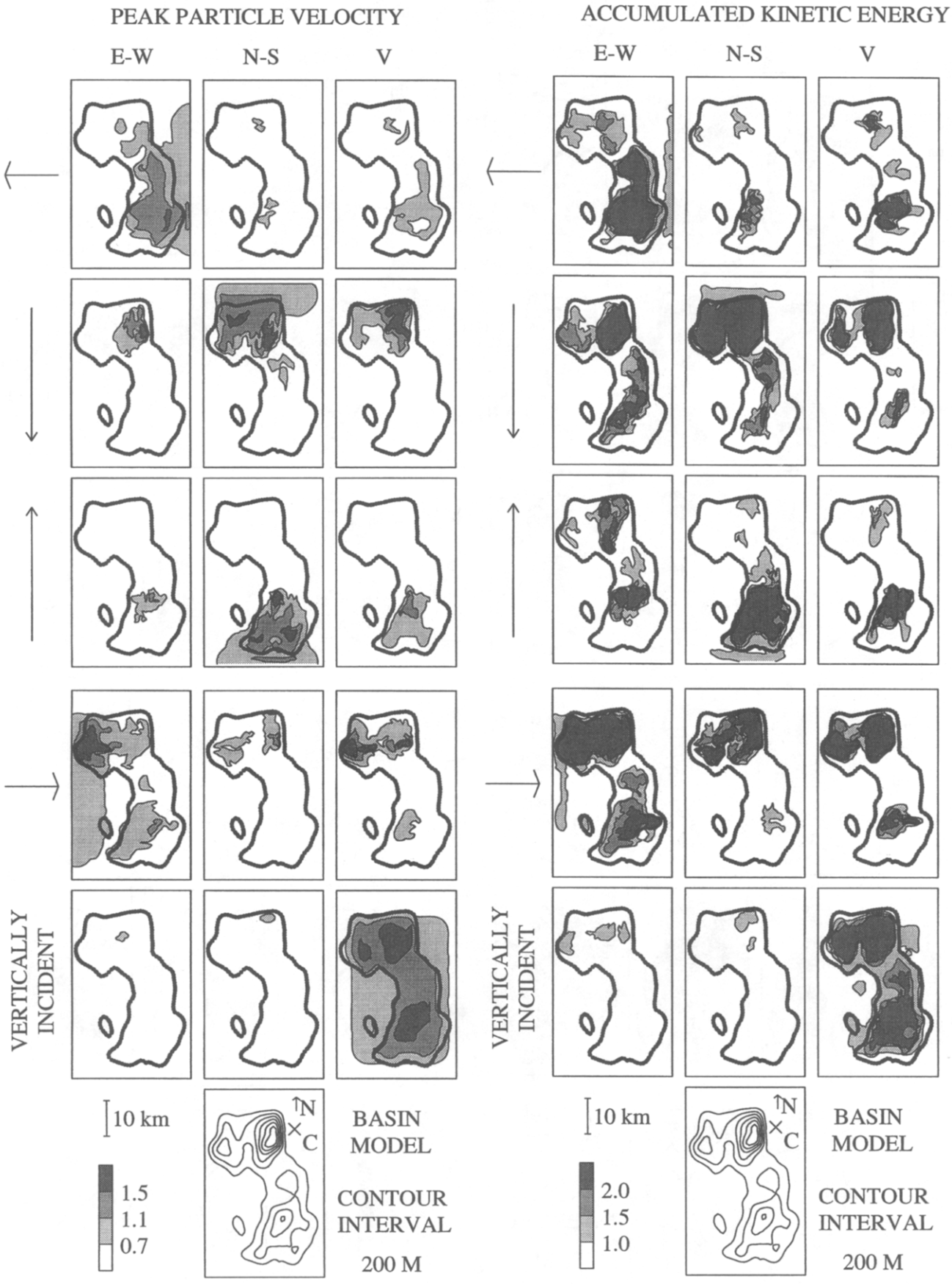
PEAK PARTICLE VELOCITY
E-W
N-S
V
ACCUMULATED KINETIC ENERGY
E-W
N-S
V
VERTICALLY INCIDENT
VERTICALLY INCIDENT
10 km
1.5
1.1
0.7
N
C
BASIN MODEL
CONTOUR INTERVAL
200 M
10 km
2.0
1.5
1.0
N
C
BASIN MODEL
CONTOUR INTERVAL
200 M

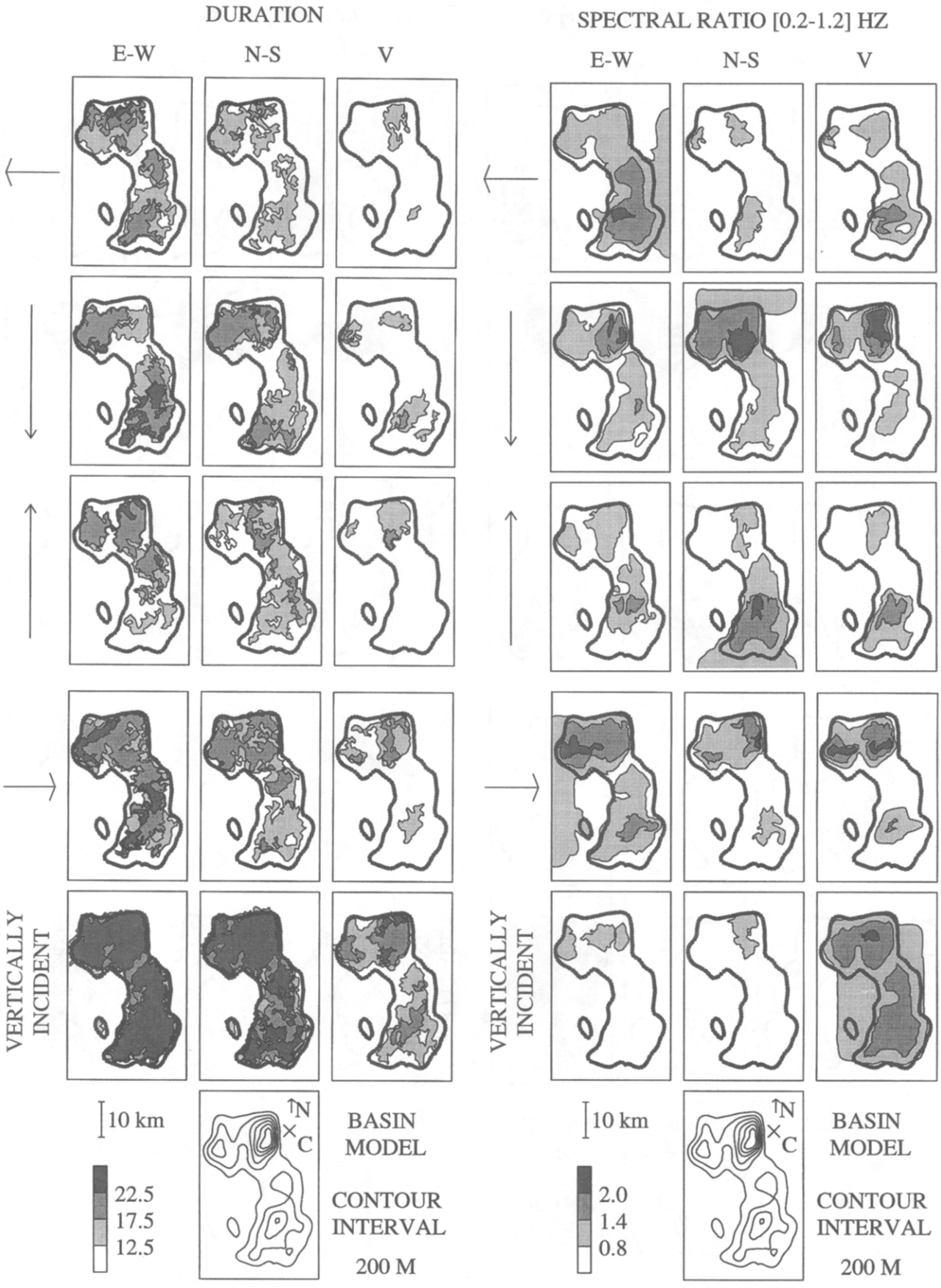
DURATION
E-W
N-S
V
SPECTRAL RATIO [0.2-1.2] HZ
E-W
N-S
V
VERTICALLY INCIDENT
VERTICALLY INCIDENT
10 km
22.5
17.5
12.5
N
C
BASIN MODEL
CONTOUR INTERVAL
200 M
10 km
2.0
1.4
0.8
N
C
BASIN MODEL
CONTOUR INTERVAL
200 M

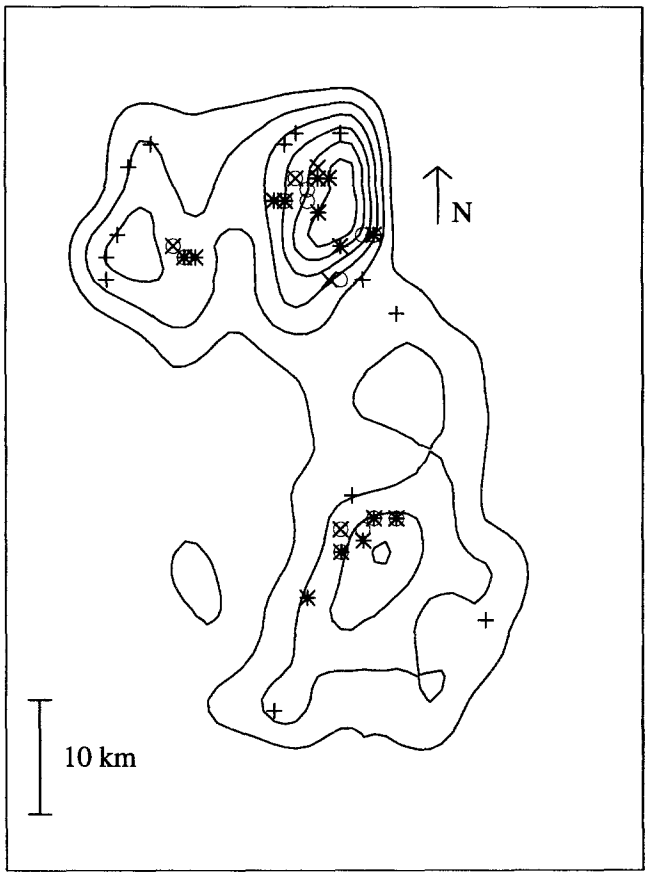

Figure 8. Location of sites associated with the largest values of the peak particle velocities (*), signal durations (+), cumulative kinetic energies (o), and spectral magnitudes (x) of each component for the five *P*-wave simulations.

peak particle velocities on the component parallel to the propagation direction to decay significantly with distance (see Appendix). Therefore, the values of these ground-motion parameters are generally larger in areas of the basin nearest the source than they are elsewhere in the basin.

The signal durations show a somewhat different pattern; these values generally increase away from the entry points. This point is illustrated in Figure 9, in which the records from the simulation with the *P* wave incident from the south are shown for sites located above the deepest points in the northern and southern parts of the basin. The longer signal duration with propagation distance is in part due to a gradually larger delay between the *P* and surface waves; however, the increase in signal duration caused by this effect is no more than 16 sec for the waves propagating from site 1 to site 2. Since the increase in signal duration at site 2 compared to site 1 is as large as 35 sec depending on the component, we conclude that scattering and mode conversion at the basin boundaries or the free surface increases the signal duration significantly.

Comparison of Simulation Results with Data

As a check on the accuracy of our 3D modeling, we compare synthetic seismograms from our simulation with the vertically incident plane *P* wave to seismograms of nearly vertically incident teleseismic *P* waves recorded at an alluvium site in the Salt Lake Valley and a nearby rock site. We use 2D simulations to evaluate the sensitivity of the 3D simulation to source incidence angle and attenuation, and to some features that could not be included in the 3D model due to computer limitations: a bedrock velocity gradient, a near-surface low-velocity layer in the basin, and topography.

Collection and Processing of Teleseismic Data

The data are from an M_b 6.0 earthquake with a focal depth of 550 km that occurred south of the Fiji Islands on 10 October 1990. We selected the data from this earthquake for comparison with our simulation because the *P* wave recorded at the rock site has an exceptionally simple waveform (Fig. 10), and its incidence angle is within 1° of the minimum incidence angle for direct *P* waves that do not travel through the earth's core: 12°, assuming an upper-crustal velocity of 5 km/sec, as in our model. The data were recorded at two temporary three-component stations of the University of Utah regional seismic network: BRO and MHD (Fig. 1a). BRO was located on Quaternary alluvium in the Salt Lake Valley. MHD was located 8 km ENE of BRO on a Cambrian quartzite outcrop in the Wasatch Range near the eastern edge of the valley. All six components of these stations had matched instrumentation that produced a relatively narrow-band velocity response peaked near 1 Hz. The complete instrument response for each component, from the seismometer through the analog telemetry to the centralized digital recording system, was determined by Erwin McPherson using an *in situ* calibration method based on the cross-spectral technique of Berger *et al.* (1979). We used the results of

Table 4
Maximum Ratios of Ground-Motion Parameters*

		Direction of *P*-Wave Source				
Component	Ground-Motion Parameter	West	South	North	East	Vertical
E–W	peak particle velocity	2.9	1.6	2.4	2.3	1.2
N–S	peak particle velocity	1.7	2.5	2.6	1.1	0.9
Vertical	peak particle velocity	2.4	1.5	2.7	1.5	1.8
E–W	cumulative kinetic energy	15.9	5.7	10.8	11.1	2.9
N–S	cumulative kinetic energy	11.1	12.1	15.2	4.0	1.8
Vertical	cumulative kinetic energy	13.7	10.7	11.5	8.7	7.5
E–W	signal duration	33.6	28.7	33.5	27.7	40.0
N–S	signal duration	19.6	26.9	29.4	24.0	39.9
Vertical	signal duration	25.1	24.6	22.1	21.6	30.7
E–W	spectral magnitude	3.5	2.1	2.9	2.4	1.6
N–S	spectral magnitude	2.7	3.1	3.3	1.6	1.2
Vertical	spectral magnitude	3.3	2.6	3.3	2.4	2.5

*The reference is taken as the value on the component parallel to the propagation direction at a rock site; for the horizontally incident *P* waves, this site is located 3 km from where the source is imposed.

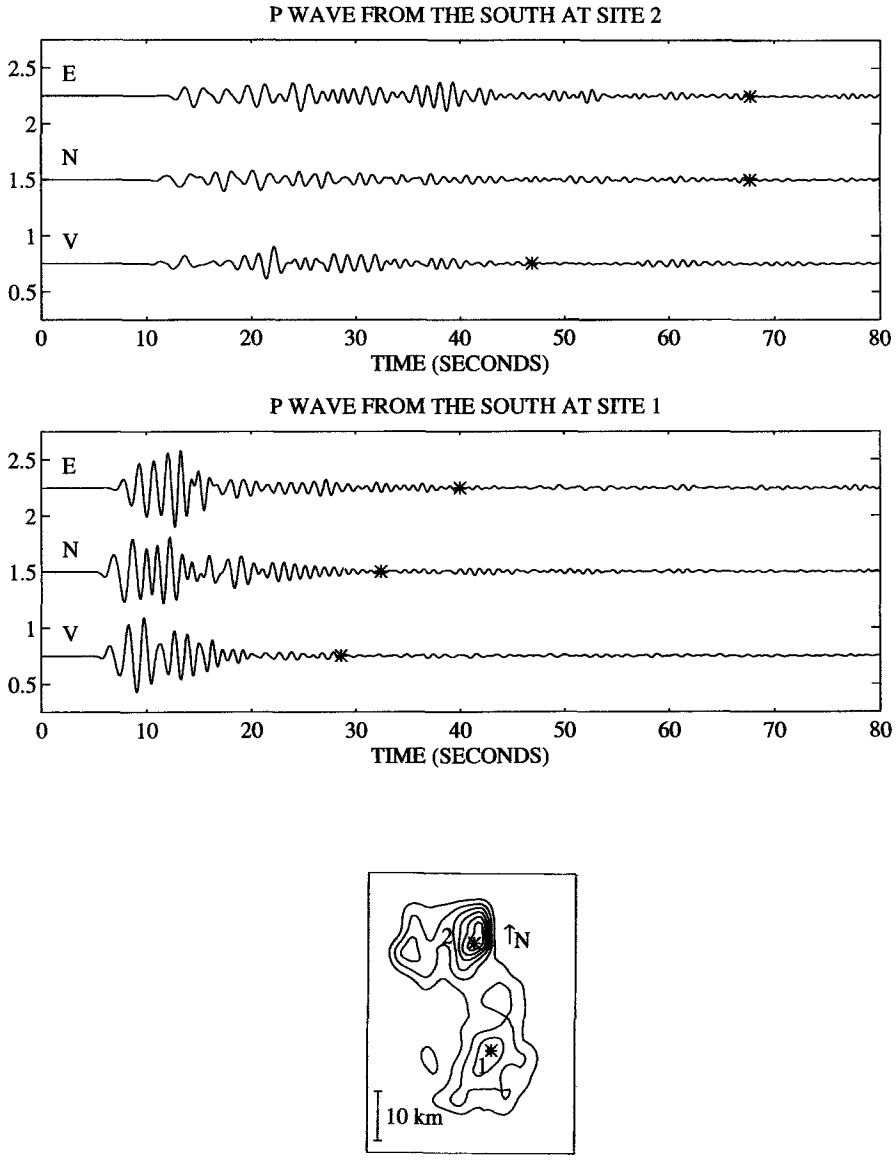

Figure 9. E–W-, N–S-, and vertical-component velocity seismograms at sites 1 and 2 shown on the map for a *P* wave incident from the south. The times when the signals reach the noise level for at least 5 sec are depicted by asterisks. The contour map shows the depth to the sediment-bedrock boundary at a contour interval of 200 m, shallowest contour at a depth of 150 m below the valley floor.

these calibrations to correct the data for the small differences (up to 20%) in the frequency responses of the six components. To correct the data, we deconvolved the measured instrument response from each trace and then convolved it with the instrument response of the vertical component at MHD.

Comparison of Observed and 3D Synthetic Waveforms

In order to allow a direct comparison between the observed and simulated velocity records, it was necessary to compensate for the effect of the (normalized) instrument response on the data and for the waveform differences between the Ricker wavelet source used in the simulations (Fig. 2) and the teleseismic *P* wave from the Fiji earthquake. This task was accomplished by convolving the simulated traces with a 60-sec-long least-squares filter designed to fit the synthetic vertical-component record at MHD to the observed vertical-component record at MHD. The key assumption underlying this procedure is that the waveform recorded on the vertical component at MHD, the rock site, is the same as the waveform of the *P* wave that entered the bedrock beneath the basin, except for the modifications caused by the instrument and the interaction with the free surface. The remarkable simplicity of the vertical-component record from MHD (Fig. 10) lends some support to this assumption.

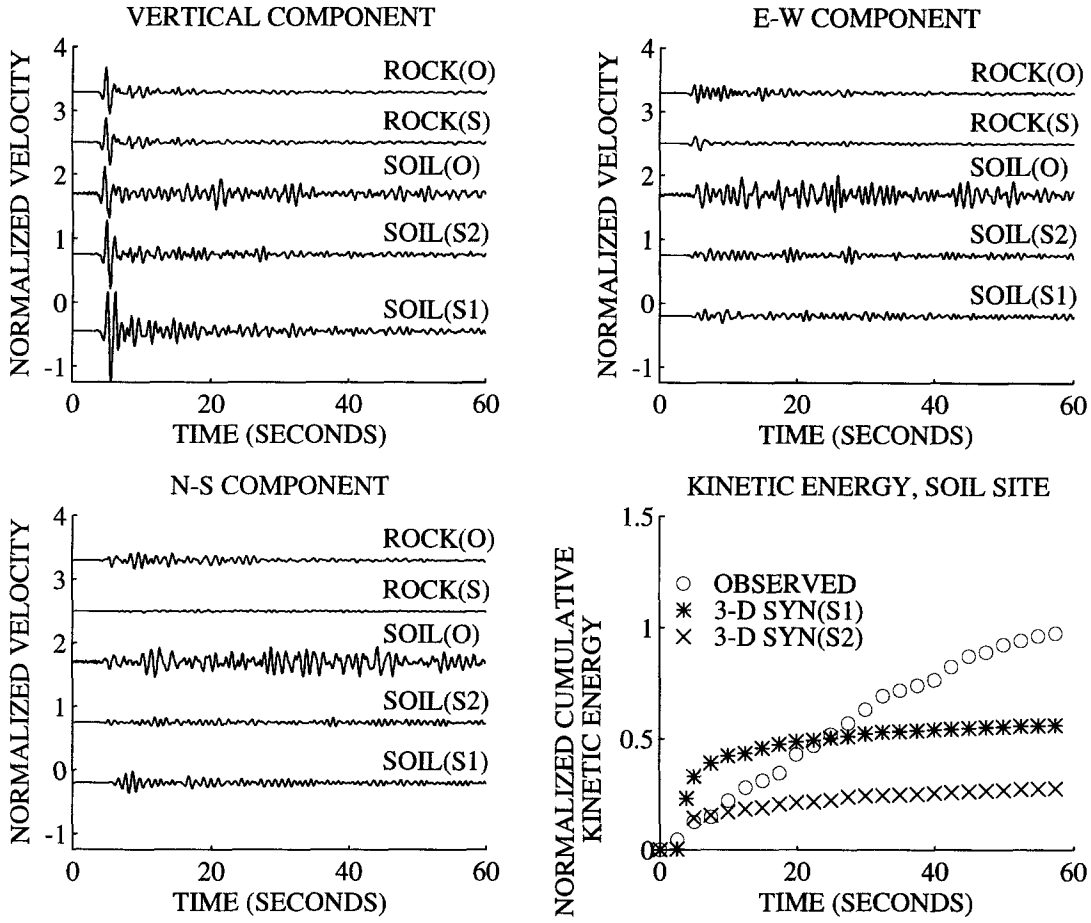

Figure 10. Comparison of observed (O) teleseismic *P* waves (incidence angle ≈12°) with 3D synthetic seismograms (S) for vertically incident plane *P* waves at sites BRO (SOIL) and MHD (ROCK) (see Fig. 1 for locations). The data are from an M_b 6.0 earthquake that occurred near the Fiji Islands on 10 October 1990 at a distance of 91° from the stations. The synthetics labeled S1 are for site BRO where the data were recorded, and those labeled S2 are for another site 3.1 km to the ESE. The graph in the lower-right panel shows plots of total cumulative kinetic energy per unit volume versus time for the BRO data (circles) and the 3D synthetics (asterisks for S1, x's for S2).

Figure 10 shows the processed versions of the observed (O) and simulated (S and S1) velocity seismograms of the Fiji event for stations BRO (SOIL) and MHD (ROCK). The graph at the lower right shows cumulative kinetic energy versus time for the data (circles) and the synthetics (asterisks) at BRO. The data for the teleseism show only about a 10% amplification of the initial *P* wave at the alluvium site compared to the rock site but considerable amplification of the *P*-wave coda, especially on the horizontal components (compare traces labeled ROCK(O) and SOIL(O) on Fig. 10).

The 3D synthetics for the alluvium site (SOIL(S1), Fig. 10) overestimate the amplification of the initial *P* wave and underestimate the amplification of the coda seen in the data traces from this site (SOIL(O)). The large amplitude of the initial *P* wave in the synthetics is due in part to constructive interference between the direct wave and a phase that reflects once off the free surface and once off the bottom of the sediments. This interference pattern is illustrated in the right-hand column of Figure 11, which shows the initial *P* wave for simulations with a series of 1D versions of our basin model with varying sediment thicknesses. The amplification of the initial *P* wave predicted by the 1D model with a sediment thickness of 0.525 km is similar to the amplification predicted by the 3D model in the vicinity of BRO, where the sediment thickness is about 0.55 km. As measured by the ratio of the peak particle velocity of the initial *P* wave to that of the initial *P* wave for a simulation with a bedrock half-space model, the amplification factor is 1.7 in the 1D case and 1.9 in the 3D case. The amplification factor for a 1D simulation with a thick (1.275 km) sediment layer is 1.47, which is in good agreement with the amplification factor of 1.46 predicted for the transmitted wave by simple plane-wave theory (see Olsen and Schuster, 1995).

The amplitude of the initial *P* wave is significantly smaller in the 3D synthetics for a site 3.1 km ESE of the recording site (S2, Figs. 10 and 11), where the sediment

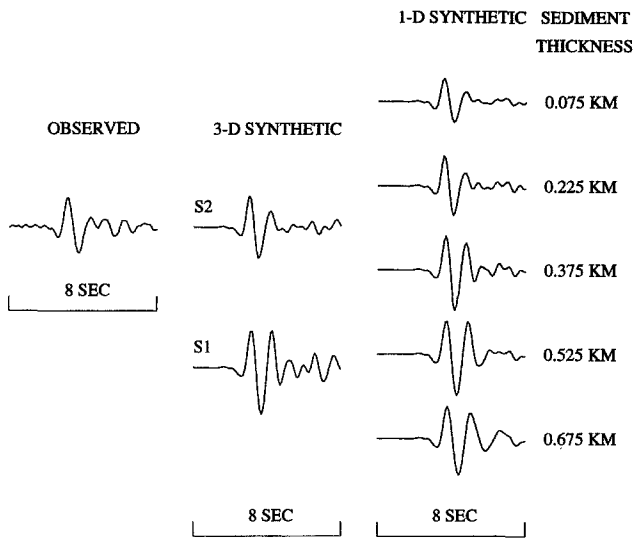

Figure 11. Illustration of the effects of sediment thickness on vertical-component synthetic seismograms for simulations with vertically incident *P* waves. Left column: vertical-component BRO recording of *P* waves from the Fiji teleseism. Middle column: 3D synthetic seismograms at BRO (S1), where the sediment thickness is about 0.55 km, and at site S2 located 3.1 km ESE of BRO, where the sediment thickness is about 0.3 km. Right column: 1D synthetic seismograms for simulations with a vertically incident *P* wave in layer-over-half-space models with varying layer thicknesses; the elastic parameters for the layer and the half-space are those of the sediments and the bedrock, respectively, in the 3D model (Table 1). The numbers at the right are the sediment thicknesses. Both the 1D and 3D synthetics are convolved with a 60-sec-long least-squares filter designed to fit the synthetic vertical-component record at rock site MHD to the observed vertical-component record at MHD.

depth is about 0.3 km instead of about 0.55 km. The weaker interference pattern produced by the thinner sediments at this site results in a synthetic *P* wave that matches the observed *P* wave from BRO in both amplitude and waveform better than the synthetic *P* wave for the actual site. These observations show that the amplitude and waveform of the initial *P* wave in the synthetics are sensitive to variations in sediment thickness that are comparable to the estimated accuracy of our 3D model (standard deviation ≈0.25 km; Radkins, 1990).

Effects of Model Deficiencies

We used 2D simulations to examine the seismic effects of some features that were not included in the 3D model, namely, topography, a near-surface velocity gradient in the bedrock, a near-surface layer of low-velocity unconsolidated sediments in the basin, and attenuation. We also used 2D simulations to determine if the 12° difference in incidence angle between the *P* waves from the Fiji teleseism and the *P* waves used in the 3D simulation could account for some of the differences between the observed and 3D synthetic seismograms at BRO. The models used for the 2D simulations were based on a cross section of the 3D model near the two recording stations (see Figs. 1 and 12; Table 5). As with the 3D simulations, each set of synthetic seismograms was convolved with a least-squares filter designed to match the synthetic vertical-component record at the rock site to the observed vertical-component record in both waveform shape and amplitude. We use plots of cumulative kinetic energy versus time for the 2D synthetics as a tool for evaluating the effects of the refinements mentioned above. This approach is justified by the similarity of the cumulative kinetic energy curves for the 3D and 2D two-layer responses, at least at site S2 (Fig. 13). We compare the observed cumulative energy curve from BRO with those calculated from the 2D synthetic records at site S2 on the cross section. Although S2 is located 2.5 km NE of the projection of BRO onto the cross section (Fig. 1), the results of the 1D and 3D modeling presented above (Fig. 11) suggest that the sediment thickness beneath S2 in our models is similar to the actual sediment thickness beneath BRO and that the sediment thickness below a site has a greater influence on site response than its distance from the edge of the basin.

In the uppermost several hundred meters of the crust, bedrock *P*-wave velocities can decrease with depth by almost a factor of 2, at least in sedimentary rocks, and V_p/V_s ratios typically increase to values of around 2.0 near the surface (e.g., Nicholson and Simpson, 1985; Moos, 1988; Williams and Arabasz, 1989). A shallow refraction survey at MHD indicated a near-surface bedrock *P*-wave velocity of 1.75 km/sec. The depth extent of this near-surface low velocity is unknown. In light of this velocity information, we modified our 2D model by assigning a linear variation of *P*-wave velocity and V_p/V_s from 1.75 km/sec and 2.0 at the surface, respectively, to 5.0 km/sec and 1.73 at a depth of 0.5 km. The effect of this bedrock velocity gradient is a slightly lower normalized cumulative kinetic energy at BRO due to increased amplitude of the initial *P* wave at the reference site (MHD) (dotted curve, Fig. 13).

In order to examine the effects of topographic scattering by the nearby mountains, we added an irregular free-surface boundary condition developed by Xu (1995) to our 2D finite-difference code. The dashed curve in Figure 13 shows the cumulative kinetic energy at S2 for the simulation with the 2D model including both the bedrock gradient and topography. It is evident that topographic scattering has little effect on the initial *P*-wave amplitude and increases the normalized cumulative kinetic energy of the whole signal only slightly (≈40%).

The near-surface unconsolidated sediments in the Salt Lake Basin were not included in our 3D model because their seismic velocities were below the practical limits dictated by the computer resources available to us for the 3D simulation. Borehole measurements made by Williams *et al.* (1993) 4.2 km west of BRO show average *P*-wave and *S*-wave velocities in the uppermost 58 m of the sediments of, respectively, 1.65 and 0.41 km/sec. In our modified 2D model, these velocities

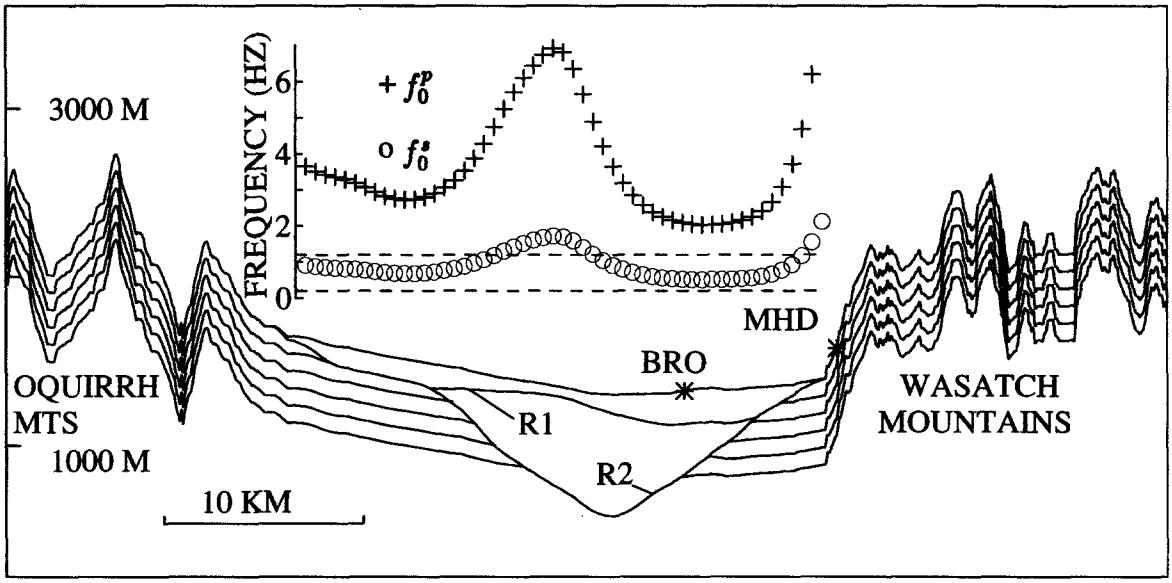

Figure 12. Vertical cross section of the Salt Lake Basin model taken along the profile shown in Figure 1b, with some additional features that were not included in the 3D simulation: a near-surface velocity gradient in the bedrock, topography, and a near-surface layer of low-velocity sediments in the basin (above R1). The contours in the 2D model depict the 1D bedrock velocity gradient of *P*-wave velocity and V_p/V_s ratio with a contour interval of 0.65 km/sec and 0.054, respectively. The pluses and circles plot the fundamental *P*-wave (f_0^p) and *S*-wave (f_0^s) vertical resonance frequencies, respectively, for the low-velocity layer along the profile. $f_0^p = V_p/4L$ and $(f_0^s) = V_s/4L$, where L is the thickness of the low-velocity layer and V_p and V_s are the layer's *P*- and *S*-wave velocities, respectively. The dashed lines mark the effective bandwidth of the Ricker wavelet source, which is 0.2 to 1.2 Hz. The 2D model parameters are listed in Table 5, and vertical exaggeration is 3.5.

Table 5
2D Model Parameters

Spatial discretization (km)	0.025
Temporal discretization (sec)	0.0021
P-wave velocity of unconsolidated sediments (km/sec)	1.65
S-wave velocity of unconsolidated sediments (km/sec)	0.41
Density of unconsolidated sediments (g/cm³)	2.0
P-wave velocity of semi-consolidated sediments (km/sec)	2.2
S-wave velocity of semi-consolidated sediments (km/sec)	1.27
Density of semi-consolidated sediments (g/cm³)	2.2
P-wave velocity of bedrock at the surface (km/sec)	1.75
S-wave velocity of bedrock at the surface (km/sec)	0.875
P-wave velocity of bedrock at depths ≥0.5 km (km/sec)	5.0
S-wave velocity of bedrock at depths ≥0.5 km (km/sec)	2.89
Density of bedrock (g/cm³)	2.6
Number of horizontal grid points	2,886
Number of vertical grid points	500
Minimum source frequency (Hz)	0.2
Maximum source frequency (Hz)	1.2
Peak source frequency (Hz)	0.6
Number of time steps	20,000
Simulation time (sec)	42

were assigned to the entire thickness of the unconsolidated sediments due to lack of information about the depth extent of these low velocities. The lower boundary of the unconsolidated sediments, R1, is a cross section along the profile on Figure 1 of a 3D surface that we obtained by interpolating lithology information taken from 531 water wells in the Salt Lake Valley (Arnow *et al.*, 1970; Fig. 1b). The cumulative kinetic energy curves at BRO for the 2D models with and without the near-surface layer of low velocities show that the amplitude of the coda is greatly enhanced by the presence of the near-surface low velocities (compare dashed curve and pluses, Fig. 13).

Using the slowness tables in Kennett (1991), we estimate that *P* waves from the Fiji event have an incidence angle of 12° from vertical (with a backazimuth of 239°) in the 5.0 km/sec bedrock beneath the basin. However, the 3D simulation was done using *P* waves with a 0° incidence angle. We examined the sensitivity of the basin response to the incidence angle by running a simulation with a 12°-incident *P* wave in the 2D model, including all the refinements mentioned above. The change in incidence angle caused a substantial increase in the amplitude of the coda, raising the cumulative kinetic energy after 60 sec of simulation by a factor of 3 (compare asterisks and pluses, Fig. 13). Various

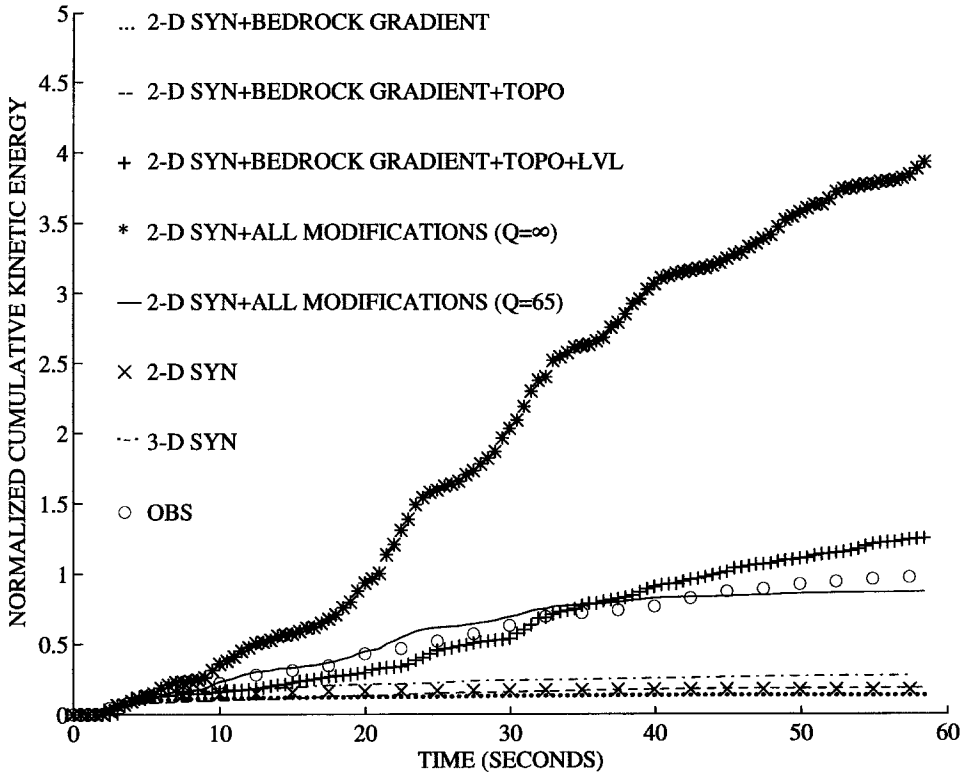

Figure 13. Plots of cumulative kinetic energy per unit volume versus time for the teleseismic P waves recorded at soil site BRO (circles), the 3D synthetics at site S2 located 3.1 km to the ESE of the recording site (dash dot), and various 2D synthetics at site S2. The 2D synthetics were computed using a vertical cross section of the two-layer 3D model (x's), and some modified versions of this model that included some or all of the following features as indicated in the key: a near-surface velocity gradient in the bedrock (BEDROCK GRADIENT), topography (TOPO), a near-surface layer of low-velocity unconsolidated sediments in the basin (LVL), an incidence angle of 12° instead of zero, and attenuation (Q = 65). The model parameters are listed in Table 5.

tests showed that this increase in coda energy was predominantly due to increased conversion of P-wave energy to S-wave energy, which becomes trapped very efficiently within the unconsolidated sediments because of the factor-of-3 S-wave velocity increase at the base of this layer. P- to S-wave conversion at the gently dipping layer boundaries in the model increases sharply when the P-wave incidence angle changes from 0° to 12°, as can be shown by calculations of plane-wave transmission and reflection coefficients for 1D-layered approximations of the basin model. For example, in a 1D basin model consisting of unconsolidated sediments overlying bedrock, no SV waves are generated by a vertically incident P wave. However, the amplitude of the SV waves generated by a 12°-incident P wave at the bedrock-unconsolidated sediment interface and by its first and second reflections off this interface are, respectively, 31%, 25%, and 19%, of that for the incident P wave. These S waves are amplified by constructive interference within the unconsolidated sediment layer, because the fundamental resonance frequencies for vertical interference of S waves in this layer are near the peak frequency (0.6 Hz) of the source (Fig. 12). In contrast, the fundamental resonance frequencies for P waves in the unconsolidated sediments are all above the effective upper end of the source bandwidth (1.2 Hz).

Figure 13 shows that after the first 5 sec, the cumulative kinetic energy produced at S2 in the 2D simulation with the bedrock gradient, topography, near-surface low-velocity layer, and correct incidence angle (asterisks) is significantly higher than that computed from the teleseismic recordings at BRO (circles). This discrepancy can be accounted for by anelastic attenuation, which was omitted in all of the simulations. We apply an approximate correction for attenuation after least-squares filtering using the formula

$$S(t) = S^{EL}(t) \cdot e^{\frac{-\pi \cdot f_p \cdot t}{Q}}, \tag{10}$$

where $S(t)$ is the corrected seismogram, $S^{EL}(t)$ is the original seismogram, t denotes time measured from the start of the simulation, f_p represents the peak frequency (0.6 Hz) of the source, and Q is the quality factor. This attenuation correction assumes that Q is the same for both P and S waves and

is uniform throughout the model. The best match between the cumulative kinetic energy curve for the data and those for synthetics computed with models including all features mentioned above was obtained for $Q = 65$ (compare circles and solid curve, Fig. 13). This average Q value is higher than the value of 20 obtained by Olsen *et al.* (1995) from 2D modeling of mine blast recordings at soil sites in the Salt Lake Valley. The differences in the Q values obtained in the two studies is probably due to differences in the propagation paths for which Q was determined.

Figure 14 compares the observed seismograms at BRO to the synthetic seismograms at S2 from the 2D two-layer simulation with vertically incident *P* waves (2-D 2-LAYER) and the 2D model simulation including all the modifications discussed above (2-D + ALL MODIFICATIONS). The latter synthetics clearly provide a better match to the data, but the match is still far from perfect. For example, compared to the data, the synthetic radial component has a lower dominant frequency and higher amplitudes near the beginning of the trace. A possible explanation for the first discrepancy is that the actual depth extent of the near-surface low velocities is less than assumed in the modified 2D basin model. A shallower limit to these low velocities would shift the *S*-wave resonance frequencies to higher values (see inset, Fig. 12), thus increasing the dominant frequency of the radial-component synthetic.

One significant feature of the teleseismic data that is reproduced by our final 2D synthetics is the fact that the coda waves are amplified more by the basin structure than are the initial *P* waves. Our simulations suggest that the large-amplitude coda observed at the alluvium site is primarily due to reverberations in near-surface unconsolidated sediments, whereas the amplification of the initial *P*-wave arrival is mostly due to the impedance decrease and resonance effects associated with the deeper basin structure. Margheriti *et al.* (1994) have recently found some observational evidence that coda waves are amplified more than direct *S* waves at soil sites and that, on average, this difference increases as the soil conditions soften. They explained their results by an increase in coda amplitude caused by entrapment of energy in the alluvial basin where their soil sites were located. If alluvial basins tend to amplify coda waves more than direct waves, as suggested by both our study and that of Margheriti *et al.* (1994), then this phenomenon should be taken into account when using empirical site amplification data to predict ground motions from large earthquakes.

Conclusions

1. Our 3D elastic simulations of *P* waves entering the Salt Lake Basin show that amplification of low-frequency ground motions tends to be greater at sites overlying the deeper parts of the basin—as measured by ratios of peak particle velocities, cumulative kinetic energies, ground-motion durations, and velocity spectra at alluvium sites relative to rock sites. The maximum values of these parameter ratios are generally found above steeply dipping walls of the basin. We find maximum ratios of 2.9 for peak particle velocities, 15.9 for cumulative kinetic energies, 40.0 for signal durations, and 3.5 for spectral magnitudes.
2. In our 3D simulations, the largest vector particle velocities are caused by *P* waves when the source is a vertically incident *P* wave and by *SV* waves when the source is a *P* wave incident from the west, south, or east. These large phases come from within 10° of the source azimuth. Lower-energy *S* and surface waves follow the strongest arrivals.
3. At an alluvium site in the southern Salt Lake Valley, synthetic seismograms from our 3D simulation with a vertically incident plane *P* wave predict more amplifi-

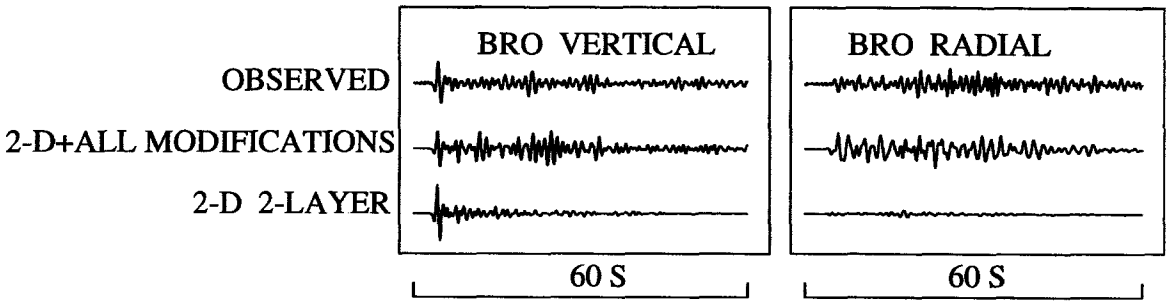

Figure 14. Comparison of vertical-component and radial-component records from BRO of steeply incident teleseismic *P* waves with 2D synthetic seismograms at S2. For both data and synthetics, the radial component is along the azimuth of the cross section. The 2D synthetics labeled "2-D 2-LAYER" are from a simulation with a vertically incident *P* wave in a model that is a vertical cross section of the two-layer 3D model along the profile shown in Figure 1. The 2D synthetics labeled "2-D + ALL MODIFICATIONS" were computed for a *P* wave with an incidence angle of 12° (as for the teleseism) in a modified version of this model illustrated in Figure 12 and corrected for attenuation ($Q = 65$).

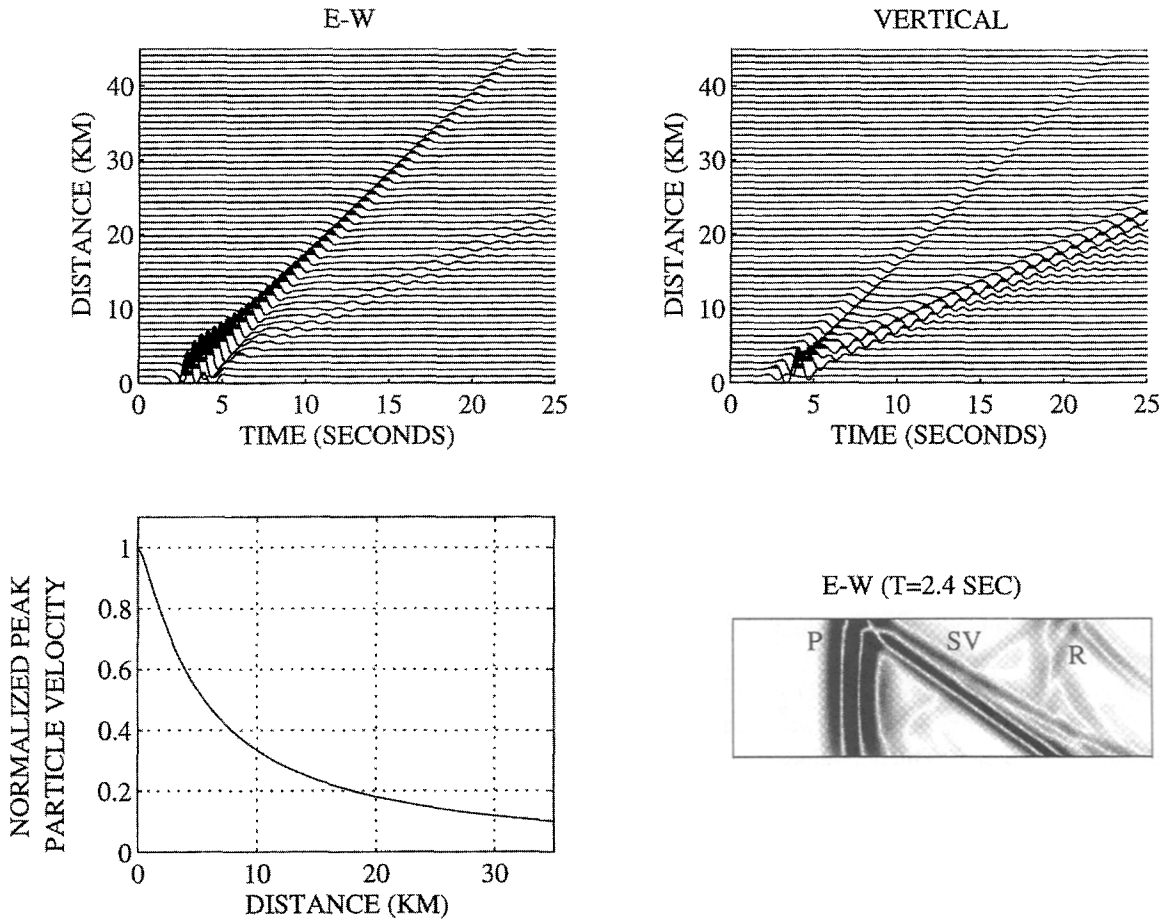

Figure 15. Illustration of pseudo-geometrical spreading for a P wave horizontally incident into a half-space with V_p = 2.20 km/sec, V_s = 1.27 km/sec, and ρ = 2.20 g/cm^3. (top) Radial- and vertical-component velocity seismograms. (bottom left) Peak particle velocity for the wave field versus distance from a point 3 km from where the source is imposed. (bottom right) Snapshot of the radial-component particle velocity after 2.4 sec of simulation; "P" denotes the P wave, "SV" denotes the SV wave, and "R" denotes the Rayleigh wave. The darkness of the shading on the snapshot is proportional to the absolute value of the radial-component particle velocity.

cation of the initial P wave and less amplification of the coda than we infer from a comparison of steeply incident teleseismic P waves recorded at this site and a nearby rock site. The large amplitude of the initial P wave in the synthetics is due in part to constructive interference between the direct wave and the reflection from the bottom of the sediments. A likely explanation of the larger-than-observed amplification of the initial P wave is an erroneously large sediment thickness in the model below the recording site. 2D simulations suggest that the discrepancy between the simulated and observed coda amplitudes is largely due to omission from the model of the near-surface low-velocity unconsolidated sediment layer and attenuation, combined with the inexact modeling of the incidence angle of the teleseism. Synthetic seismograms from a 2D simulation including these features (with Q = 65), plus topography and a near-surface velocity gradient in the bedrock, provide a better match to the data than the synthetic seismograms computed with the simple two-layer 3D model.

4. Our results suggest that, for steeply incident P-wave sources, the dominant contributors to low-frequency ground-motion amplification in the Salt Lake Basin are the low impedance of the basin sediments, mode conversion, reverberations in the semi-consolidated and especially the unconsolidated sediment layers, and attenuation. Resonance of converted S waves in the unconsolidated sediments of our 2D basin model triples the cumulative kinetic energy after 60 sec of simulation using a 12°-incident P-wave source. This finding suggests that simple 1D modeling of vertically incident P waves in the unconsolidated sediments would seriously underestimate ground motions in the Salt Lake Valley caused by obliquely incident P waves.

5. Simulations in realistic 2D models may provide satisfactory predictions of low-frequency ground-motion amplification in the Salt Lake Basin. To be realistic, these models must include attenuation and the near-surface layer of low-velocity, unconsolidated sediments.

Acknowledgments

We are grateful to Erwin McPherson for engineering the installation of the two temporary seismic stations used in this study; to Ken Whipp, Jackie Bott, Susan Olig, and Suzanne Hecker for their help with the associated field work; and to Mr. and Mrs. Wesley Bromley and Mr. and Mrs. Jack Gordon for allowing the stations to be operated on their property. We acknowledge Jinlong Xu for permission to use his 2D elastic finite-difference code capable of handling topography at the free surface. Brian Bone of IBM helped to optimize the 3D finite-difference code. Thanks to Dan Trentman for helping with computer-related problems. The University of Utah Supercomputing Institute (USI) provided the CPU time required for the 3D simulations on an IBM 3090 supercomputer. The data collection and analysis were supported by the U.S. Geological Survey, Department of the Interior, under Award Number 14-08-0001-G1762, and by the State of Utah. The numerical modeling was supported by the National Science Foundation under Grant Number EAR-8816437 and EAR-9104866.

References

Adan, S. M. and K. M. Rollins (1993). Damage potential index mapping for Salt Lake Valley, Utah, *Utah Geol. Surv. Misc Pub. 93-4,* 64 pp.

Aki, K. and P. G. Richards (1980). *Quantitative Seismology Theory and Methods,* Vol. I, Freeman and Co., New York.

Anderson, J. G., P. Bodin, J. N. Brune, J. Prince, S. K. Singh, R. Quaas, and M. Onate (1986). Strong ground motion from the Michoacan, Mexico, earthquake, *Science* **233,** 1043–1049.

Arnow, T., R. Van Horn, and R. LaPray (1970). The Pre-Quaternary surface in the Jordan Valley, Utah, *U.S. Geol. Surv. Profess. Pap. 700-D,* D257–D261.

Bard, P.-Y. and M. Bouchon (1980a). The seismic response of sediment-filled valleys. Part 1. The case of incident SH waves, *Bull. Seism. Soc. Am.* **70,** 1263–1286.

Bard, P.-Y. and M. Bouchon (1980b). The seismic response of sediment-filled valleys. Part 2. The case of incident P-SV waves, *Bull. Seism. Soc. Am.* **70,** 1921–1941.

Benz, H. and R. B. Smith (1988). Elastic-wave propagation and site amplification in the Salt Lake Valley, Utah, from simulated normal faulting earthquakes, *Bull. Seism. Soc. Am.* **78,** 1851–1874.

Berger, J., D. C. Agnew, R. L. Parker, and W. E. Farrell (1979). Seismic system calibration: 2. Cross-spectral calibration using random binary signals, *Bull. Seism. Soc. Am.* **69,** 271–288.

Frankel, A., S. Hough, P. Friberg, and R. Busby (1991). Observations of Loma Prieta aftershocks from a dense array in Sunnyvale, California, *Bull. Seism. Soc. Am.* **81,** 1900–1922.

Frankel, A. and J. Vidale (1992). A three-dimensional simulation of seismic waves in the Santa Clara Valley, California, from a Loma Prieta aftershock, *Bull. Seism. Soc. Am.* **82,** 2045–2074.

Frankel, A. (1993). Three-dimensional simulations of ground motions in the San Bernardino Valley, California, for hypothetical earthquakes on the San Andreas Fault, *Bull. Seism. Soc. Am.* **83,** 1020–1041.

Gori, P. L. and W. W. Hays (1992). Assessment of Regional Earthquake Hazards and Risk Along the Wasatch Front, Utah, *U.S. Geol. Surv. Profess. Pap. 1500-A-J.*

Hill, J., H. Benz, M. Murphy, and G. T. Schuster (1990). Propagation and resonance of SH waves in the Salt Lake Valley, Utah, *Bull. Seism. Soc. Am.* **80,** 23–42.

Kawase, H. and K. Aki (1989). A study on the response of a soft basin for incident S, P and Rayleigh waves with special reference to the long duration observed in Mexico City, *Bull. Seism. Soc. Am.* **79,** 1361–1382.

Kennett, B. L. N. (1991). IASPEI 1991 Seismological Tables, Research School of Earth Sciences, Australian National University, Canberra.

Levander, A. R. (1988). Fourth-order finite-difference P-SV seismograms, *Geophysics* **53,** 1425–1436.

Margheriti, L., L. Wennerberg, and J. Boatwright (1994). A comparison of coda and S-wave spectral ratios as estimates of site response in the southern San Francisco Bay area, *Bull. Seism. Soc. Am.,* **84,** 1815–1830.

Moos, D. (1988). The effects of mylonitization and fractures on elastic wave velocities in crystalline rock—examples from the Cajon Pass scientific drillhole, *Geophys. Res. Lett.* **15,** 1053–1056.

Murphy, M. (1989). Finite-difference simulation of seismic P- and SV-wave amplification in the Salt Lake Valley, Utah, *Master's Thesis,* University of Utah, Salt Lake City, Utah, 114 p.

Nicholson, C. and D. W. Simpson (1985). Changes in V_p/V_s with depth: implications for appropriate velocity models, improved earthquake locations, and material properties of the upper crust, *Bull. Seism. Soc. Am.* **75,** 1105–1123.

Olsen, K. B. (1994). Simulation of three-dimensional wave propagation in the Salt Lake Basin, *Ph.D. Thesis,* University of Utah, Salt Lake City, Utah, 157 p.

Olsen, K. B. and G. T. Schuster (1995). Causes of low-frequency ground motion amplification in the Salt Lake Basin: the case of the vertically-incident P wave, *Geophys. J. Int.,* in press.

Olsen, K. B., J. C. Pechmann, and G. T. Schuster (1995). An analysis of simulated and observed blast records in the Salt Lake Basin, *Bull. Seism. Soc. Am.,* submitted.

Radkins, H. (1990). Bedrock topography of the Salt Lake Valley, Utah, from constrained inversion of gravity data, *Master's Thesis,* University of Utah, Salt Lake City, Utah, 59 p.

Stacey, F. D. (1992). *Physics of the Earth,* Brookfield Press, Brisbane, Australia, 511 p.

U.S. Geological Survey Staff (1990). The Loma Prieta, California, earthquake: an anticipated event, *Science* **247,** 286–293.

Vidale, J. E. and D. V. Helmberger (1988). Elastic finite-difference modeling of the 1971 San Fernando, California, earthquake, *Bull. Seism. Soc. Am.* **78,** 122–141.

Williams, D. J. and W. J. Arabasz (1989). Mining-related and tectonic seismicity in the East Mountain Area Wasatch Plateau, Utah, *Pageoph* **129,** 345–368.

Williams, R. A., K. W. King, and J. C. Tinsley (1993). Site response estimates in Salt Lake Valley, Utah, from borehole seismic velocities, *Bull. Seism. Soc. Am.* **83,** 862–889.

Wong, I. G. and W. J. Silva (1993). Site-specific strong ground motion estimates for the Salt Lake Valley, Utah, *Utah Geol. Surv. Misc. Pub. 93-9,* 34 pp.

Xu, J. (1995). Implementation of free-surface boundary conditions for finite-difference solutions to the wave equation, *Master's Thesis,* University of Utah, Salt Lake City, Utah (in progress).

Yomogida, K. and J. T. Etgen (1993). 3-D wave propagation in the Los Angeles Basin for the Whittier-Narrows Earthquake, *Bull. Seism. Soc. Am.* **83,** 1325–1344.

Appendix: Pseudo-geometrical Spreading

The variation of ground-motion parameters computed for the simulations with horizontally incident P waves presented in this article is caused by a combination of azimuthally dependent basin effects and pseudo-geometrical spreading. The pseudo-geometrical spreading is due to the generation of an SV wave by the interaction of the horizontally propagating P wave with the free surface; the effect is

a loss of *P*-wave energy caused by the transfer of energy from the *P* wave to the *SV* wave, which propagates downward away from the free surface.

We simulate a plane *P* wave horizontally incident into a half-space with $V_p = 2.20$ km/sec, $V_s = 1.27$ km/sec, and $\rho = 2.20$ g/cm^3 (the elastic parameters used for the sediments in the 3D simulations) to compute the contribution from pseudo-geometrical spreading to the decrease in peak particle velocity. Figure 15 (top) shows the radial- and vertical-component velocity seismograms from the simulation; the source is imposed at zero distance. The transverse component contains no energy and is not shown. The seismograms show a *P* wave and a Rayleigh wave, both generated by the source function; the peak particle velocity of the *P* wave decays with distance from the source. Figure 15 (bottom left) shows that the *P*-wave peak particle velocity decays nonlinearly by 90% during propagation through 35 km of basin sediments, beginning at a reference site (shown at zero distance in the figure) located 3 km from the source. Ground-motion parameters calculated for rock sites located 3 km from the sources are used to normalize the ground-motion parameters determined from our simulations with horizontally incident *P* waves.

Figure 15 (bottom right) shows a velocity snapshot on the radial component after 2.4 sec of simulation. In addition to the *P* wave and Rayleigh wave apparent in the seismograms (Fig. 15, top), the snapshot shows the *SV* wave generated by mode conversion of the *P* wave at the free surface. The angle between the free-surface and the *SV* wave is 35°, as predicted from Snell's Law and the elastic parameters of the half-space.

Department of Geology and Geophysics
University of Utah
Salt Lake City, UT 84112

Manuscript received 16 August 1994.